Planck 2013 results. IV. Low Frequency Instrument beams and window functions

Planck Collaboration,; Aghanim, N.; Armitage-Caplan, C.; Arnaud, M.; Ashdown, M.; Atrio-Barandela, F.; Aumont, J.; Baccigalupi, C.; Banday, A. J.; Barreiro, R. B.

Total number of authors:
209

Published in:
ArXiv Astrophysics e-prints

Publication date:
2013

Document Version
Publisher's PDF, also known as Version of record

Astronomy & Astrophysics manuscript no. P02d˙LFI˙Beams˙2013
March 22, 2013

Planck 2013 results. IV. Low Frequency Instrument beams and window functions

Planck Collaboration: N. Aghanim[57], C. Armitage-Caplan[88], M. Arnaud[71], M. Ashdown[68,6], F. Atrio-Barandela[17], J. Aumont[57], C. Baccigalupi[82], A. J. Banday[91,8], R. B. Barreiro[64], E. Battaner[92], K. Benabed[58,90], A. Benoît[55], A. Benoit-Lévy[24,58,90], J.-P. Bernard[8], M. Bersanelli[33,47], P. Bielewicz[91,8,82], J. Bobin[71], J. J. Bock[66,9], A. Bonaldi[67], J. R. Bond[7], J. Borrill[12,85], F. R. Bouchet[58,90], M. Bridges[68,6,61], M. Bucher[1], C. Burigana[46,31], R. C. Butler[46], J.-F. Cardoso[72,1,58], A. Catalano[73,70], A. Chamballu[71,14,57], L.-Y Chiang[60], P. R. Christensen[79,36], S. Church[87], S. Colombi[58,90], L. P. L. Colombo[23,66], B. P. Crill[66,80], A. Curto[6,64], F. Cuttaia[46], L. Danese[82], R. D. Davies[67], R. J. Davis[67], P. de Bernardis[32], A. de Rosa[46], G. de Zotti[43,82], J. Delabrouille[1], C. Dickinson[67], J. M. Diego[64], H. Dole[57,56], S. Donzelli[47], O. Doré[66,9], M. Douspis[57], X. Dupac[38], G. Efstathiou[61], T. A. Enßlin[76], H. K. Eriksen[62], F. Finelli[46,48], O. Forni[91,8], M. Frailis[45], E. Franceschi[46], T. C. Gaier[66], S. Galeotta[45], K. Ganga[1], M. Giard[91,8], Y. Giraud-Héraud[1], J. González-Nuevo[64,82], K. M. Górski[66,94], S. Gratton[68,61], A. Gregorio[34,45], A. Gruppuso[46], F. K. Hansen[62], D. Hanson[77,66,7], D. Harrison[61,68], S. Henrot-Versillé[69], C. Hernández-Monteagudo[11,76], D. Herranz[64], S. R. Hildebrandt[9], E. Hivon[58,90], M. Hobson[6], W. A. Holmes[66], A. Hornstrup[15], W. Hovest[76], K. M. Huffenberger[93], T. R. Jaffe[91,8], A. H. Jaffe[53], J. Jewell[66], W. C. Jones[26], M. Juvela[25], P. Kangaslahti[66], E. Keihänen[25], R. Keskitalo[21,12], K. Kiiveri[25,41], T. S. Kisner[75], J. Knoche[76], L. Knox[27], M. Kunz[16,57,3], H. Kurki-Suonio[25,41], G. Lagache[57], A. Lähteenmäki[2,41], J.-M. Lamarre[70], A. Lasenby[6,68], R. J. Laureijs[39], C. R. Lawrence[66], J. P. Leahy[67], R. Leonardi[38], J. Lesgourgues[89,81], M. Liguori[30], P. B. Lilje[62], V. Lindholm[25,41], M. Linden-Vørnle[15], M. López-Caniego[64], P. M. Lubin[28], J. F. Macías-Pérez[73], D. Maino[33,47], N. Mandolesi[46,5,31], M. Maris[45], D. J. Marshall[71], P. G. Martin[7], E. Martínez-González[64], S. Masi[32], S. Matarrese[30], F. Matthai[76], P. Mazzotta[35], P. R. Meinhold[28], A. Melchiorri[32,49], L. Mendes[38], A. Mennella[33,47], M. Migliaccio[61,68], S. Mitra[52,66], A. Moneti[58], L. Montier[91,8], G. Morgante[46], D. Mortlock[53], A. Moss[84], D. Munshi[83], P. Naselsky[79,36], P. Natoli[31,4,46], C. B. Netterfield[19], H. U. Nørgaard-Nielsen[15], D. Novikov[53], I. Novikov[79], I. J. O'Dwyer[66], S. Osborne[87], F. Paci[82], L. Pagano[32,49], D. Paoletti[46,48], B. Partridge[40], F. Pasian[45], G. Patanchon[1], O. Perdereau[69], L. Perotto[73], F. Perrotta[82], E. Pierpaoli[23], D. Pietrobon[66], S. Plaszczynski[69], P. Platania[65], E. Pointecouteau[91,8], G. Polenta[4,44], N. Ponthieu[57,50], L. Popa[59], T. Poutanen[41,25,2], G. W. Pratt[71], G. Prézeau[9,66], S. Prunet[58,90], J.-L. Puget[57], J. P. Rachen[20,76], R. Rebolo[63,13,37], M. Reinecke[76], M. Remazeilles[57,1], S. Ricciardi[46], T. Riller[76], G. Rocha[66,9], C. Rosset[1], G. Roudier[1,70,66], J. A. Rubiño-Martín[63,37], B. Rusholme[54], M. Sandri*[46], D. Santos[73], D. Scott[22], M. D. Seiffert[66,9], E. P. S. Shellard[10], L. D. Spencer[83], J.-L. Starck[71], V. Stolyarov[6,68,86], R. Stompor[1], F. Sureau[71], D. Sutton[61,68], A.-S. Suur-Uski[25,41], J.-F. Sygnet[58], J. A. Tauber[39], D. Tavagnacco[45,34], L. Terenzi[46], L. Toffolatti[18,64], M. Tomasi[47], M. Tristram[69], M. Tucci[16,69], J. Tuovinen[78], M. Türler[51], G. Umana[42], L. Valenziano[46], J. Valiviita[41,25,62], B. Van Tent[74], J. Varis[78], P. Vielva[64], F. Villa[46], N. Vittorio[35], L. A. Wade[66], B. D. Wandelt[58,90,29], A. Zacchei[45], and A. Zonca[28]

(Affiliations can be found after the references)

Preprint online version: March 22, 2013

ABSTRACT

This paper presents the characterization of the in-flight beams, the beam window functions and the associated errors for the *Planck* Low Frequency Instrument (LFI). Knowledge of the beam profiles is the key to determining their imprint on the transfer function from the observed to the actual sky anisotropy power spectrum. The main beam distortions affect the beam window function, complicating the reconstruction of the anisotropy power spectrum at high multipoles, whereas the sidelobes affect the low and intermediate multipoles. The in-flight assessment of the LFI main beams relied on the measurements performed during Jupiter observations. By stacking the data from Jupiter transits, the main beam profiles are measured down to –20 dB at 30 and 44 GHz, and down to –25 dB at 70 GHz. The main beam solid angles are determined to better than 0.2% at each LFI frequency band. To ensure a characterization of the main beam free from the radiometer noise, a dedicated tuning on the *Planck* pre-launch optical model is performed. This approach provides an optical model whose beams fully reproduce the measurements in the main beam region, but also allow us to describe the beams at power levels lower than can be reached by the Jupiter measurements themselves. The agreement between the simulated beams and the scanning beams is better than 1% at each LFI frequency band. The simulated beams are used for the computation of the window functions for the effective beams. The error budget in the window functions was estimated considering both main beam and sidelobe contributions, as well as taking into account the radiometer bandshapes. The total uncertainties in the effective beam window functions are: (at $\ell \approx 600$) 2% and 1.2% at 30 and 44 GHz, respectively; and at $\ell \approx 1000$, 0.7% at 70 GHz.

Key words. methods: data analysis - cosmology: cosmic microwave background - instrument: optics

1. Introduction

This paper, one of a set associated with the 2013 release of data from the *Planck*[1] mission (Planck Collaboration I 2013), describes the beams and window functions of the Low Frequency Instrument (LFI).

Detailed knowledge of the instrumental angular response is a key requirement for the analysis of high precision measurements of the cosmic microwave background (CMB). Current genera-

* Corresponding author: M. Sandri, sandri@iasfbo.inaf.it

[1] *Planck* (http://www.esa.int/Planck) is a project of the European Space Agency (ESA) with instruments provided by two scientific consortia funded by ESA member states (in particular the lead countries France and Italy), with contributions from NASA (USA) and telescope reflectors provided by a collaboration between ESA and a scientific consortium led and funded by Denmark.

tion of experiments employ multi-frequency focal plane arrays whose off-axis beams necessarily deviate, to some extent, from an ideal, symmetric, Gaussian shape. The radiation patterns of every individual detector and their projected angular locations need to be reconstructed with great precision to avoid significant systematic effects in the data (Hill et al. 2009; Nolta et al. 2009; Huffenberger et al. 2010).

The *Planck* optical system is designed to ensure high image quality over a wide field of view, for detectors spanning over 1.5 decades in wavelength (Tauber et al. 2010). The LFI optical layout is composed of an array of 11 corrugated feed horns, each coupled to an orthomode transducer which divides the incoming electromagnetic wave into two orthogonal, linearly polarized components. Thus LFI is observing the sky with 11 pairs of beams associated with the 22 pseudo-correlation radiometers. Each beam of the pair is named `LFIXXM` or `LFIXXS` for the two polarization states (Main Arm and Side Arm of the orthomode transducer, respectively). Here `XX` is the radiometer chain assembly number, ranging from `18` to `28`. The beams from `LFI18` to `LFI23` are in the V–band (nominally from 63 to 77 GHz); we refer to them as 70 GHz. The beams from `LFI24` to `LFI26` are in the Q–band (from 39.6 to 48.4 GHz); we refer to them as 44 GHz. The beams `LFI27` and `LFI28` are in the Ka–band (from 27 to 33 GHz); we refer to them as 30 GHz. The optimization of the LFI optical system leading to the focal plane configuration used in flight is described in Sandri et al. (2010), while the preliminary characterisation of the LFI beams based on the first in-flight data are reported in Mennella et al. (2011) and Zacchei et al. (2011).

The LFI map-making procedure does not take into account the beam profile, which is effectively assumed to be a pencil beam. To correct for the beam shape, the angular power spectrum computed from the observed map is divided by the *beam window function* to reveal the intrinsic angular power spectrum of the sky. For this reason, beam knowledge directly affects the cosmological analyses. Typically, the beam should be mapped to less than –30 dB of the peak to achieve 1% accuracy on the angular power spectrum (Page et al. 2003). By stacking the data from the first four Jupiter transits, the LFI beams have been measured down to –20 dB at 30 and 44 GHz, and down to –25 dB at 70 GHz with an uncertainty of about 0.3% on the angular resolution and about 0.5% on the main beam ellipticity. In order to achieve the beam knowledge at lower power levels and improve the accuracy on the angular power spectrum, a substantial effort has been made to tune the *Planck* optical model, presented in Tauber et al. (2010), to fit the in-flight measurements of the LFI beams. This ensures a good representation of the LFI optics, both in terms of *main beam* and *sidelobes*. The separation of the instrumental angular response into main beam and sidelobes can be somewhat arbitrary. In the framework of this paper, we consider three regions defined with respect to the beam line-of-sight and reported in Fig. 1:

1. the *main beam*, which is defined as extending to 1.9, 1.3, and 0.9° at 30, 44, and 70 GHz, respectively;
2. the *near sidelobes*, which are defined as extending between the main beam angular limit and 5°;
3. the *far sidelobes*, which are defined as the beam response more than 5° from the line-of-sight.

Almost all the power falls into the main beam region (more than 99%). The collected power coming from the region outside the main beam is called *straylight* and it is one of the major sources of systematic effects in *Planck* observations, and in CMB experiments in general. Straylight impacts the measured signal essentially in two ways: (i) through direct contamination; and (ii) in the photometric calibration of the radiometer detected signal. The predicted straylight contamination has been detected in the LFI maps, and is reported in the companion paper Planck Collaboration III (2013). We would like to emphasize that, since no direct measurement of LFI sidelobes was performed in-flight, an accurate knowledge of the main beams provides a crucial means, though indirect, to quantify the straylight contamination, as the sidelobes can be estimated by fitting the electromagnetic model to the main beam data.

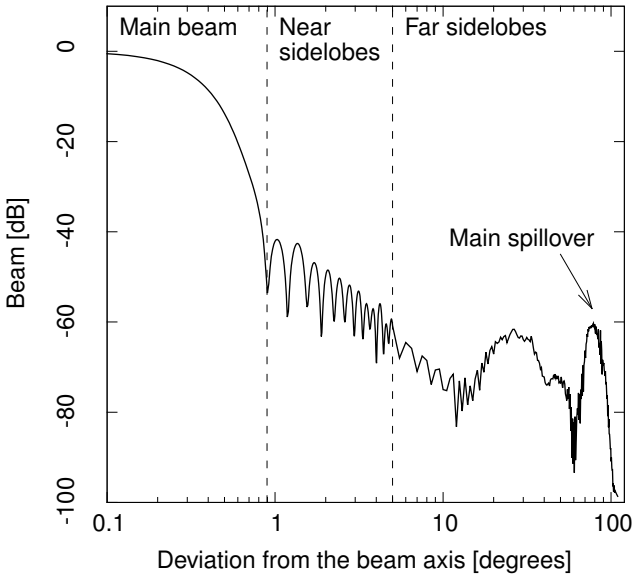

Fig. 1. Typical shape of a 30 GHz beam (`LFI27M`). The plot shows the distinction between the main beam, near sidelobes and far sidelobes. The distinction between "near" and "far" sidelobes is of course arbitrary: we mark their boundary at 5°. The peak of the spillover of the primary mirror is clearly visible, at an angle of roughly 90°.

For the clarity of the present paper and for consistency with the *Planck* companion papers, we need to make clear three important definitions: optical beams; scanning beams; and effective beams. The *optical beam* is the optical response of the feed horn coupled to the telescope. It is independent both from the radiometer response (bandshape and non-linearity) and from the satellite motion (spinning and scanning strategy). It represents the pure optical transfer function. The main beam properties of the optical beams can be evaluated using optical simulations performed with methods largely validated by ground measurements. The *scanning beam* is the beam that can be directly measured in-flight using planet observations. It derives from the optical beam coupled with the radiometer response, and smeared by the satellite motion. So, with respect to the optical beams, the scanning beams have slightly larger angular resolution, ellipticity, and solid angle. The *effective beam* is a beam defined in the map-domain, and is obtained by averaging the scanning beams pointing at a given pixel of the sky map, by taking into account the scanning strategy and the orientation of the beams themselves when they point along the direction to that pixel. Therefore, whereas for each radiometer there is one corresponding optical and scanning beam, the same radiometer has as many effective beams as the pixels of the observed sky map. The importance of the effective beams is two-fold: they are used in the window function computation; and the solid angles of the ef-

Table 1. Approximate dates of the Jupiter observations. The periods include the scan by the entire LFI field of view.

Jupiter transit	Date	OD
Scan 1 (J1)	21/10/09 – 05/11/09	161 – 176
Scan 2 (J2)	27/06/10 – 12/07/10	410 – 425
Scan 3 (J3)	03/12/10 – 18/12/10	569 – 584
Scan 4 (J4)	30/07/11 – 08/08/11	808 – 817

fective beams must be considered in the estimation of the flux density of point sources.

The data analysis pipeline, which starts from Jupiter observations and flows down to the window function characterization, is discussed in this paper according to the following outline: Sect. 2 describes the scanning beams as measured in the first four Jupiter transits, and the simulations which provide their best-fit model; Sect. 3 describes the effective beams, calculated using the simulated beams and taking into account the *Planck* scanning strategy; in Sect. 4 we present the LFI window functions. An estimate of the propagation of beam uncertainties to the beam window functions is reported in Sect. 5. In this section we also report the impact of the near and far sidelobes to the window function. For the present data release we do not correct the beam window function for the sidelobes. Instead their effect is added to the total error budget. For the next data release, we plan to include a detailed analysis carried out with the in-band integrated beams (main beam and sidelobes) that will be included in the data reduction pipeline, both in the calibration and in the window function estimation. Finally, in Sect. 6 we summarize our conclusions.

2. Scanning Beams

Jupiter is the best source in the sky for mapping the LFI beams with a high signal to noise ratio. The brightness temperature of the planet is close to 150 K and gives an antenna temperature from 40 to 350 mK depending on frequency, when the dilution factor of the beams is accounted for. Because the signal is expected to be unpolarized at LFI frequencies, the detector output (in antenna temperature T_A) is proportional to the power function of the beam as follows:

$$T_A(\theta,\phi)^M \propto |E(\theta,\phi)^M_{cp}|^2 + |E(\theta,\phi)^M_{xp}|^2 + + \left\{\chi^{OMT}\cdot\left[|E(\theta,\phi)^S_{cp}|^2 + |E(\theta,\phi)^S_{xp}|^2\right]\right\} \quad (1)$$

$$T_A(\theta,\phi)^S \propto |E(\theta,\phi)^S_{cp}|^2 + |E(\theta,\phi)^S_{xp}|^2 + + \left\{\chi^{OMT}\cdot\left[|E(\theta,\phi)^M_{cp}|^2 + |E(\theta,\phi)^M_{xp}|^2\right]\right\}, \quad (2)$$

where $E(\theta,\phi)^{M,S}_{cp}$ and $E(\theta,\phi)^{M,S}_{xp}$ are respectively the co-polar and cross-polar electric field components of the beam in the M-radiometer and S-radiometer, computed in the main beam frame ($\theta = \theta_{MB}$ and $\phi = \phi_{MB}$); and χ^{omt} is the OMT cross-polarization. This parameter was measured during the hardware development (D'Arcangelo et al. 2009) and is always less than −25 dB over the operational bandwidth, so that the terms between the curly brackets are considered negligible. To assess the beam properties we used four Jupiter transits named "J1", "J2", "J3", and "J4". Table 1 reports the date and the corresponding observational day of each transit.

2.1. Planet Data Handling

The LFI in-flight main beam reconstruction is based on a minimisation code described in Burigana et al. (2001) and incorporated into the Level 2 *Planck* LFI DPC pipeline. The code exploits the calibrated timelines corresponding to the Jupiter transits on the LFI beams, and performs a fit of the beam shape with an elliptical Gaussian function. With this Gaussian approximation, we have defined the angular resolution in terms of the full width half maximum (FWHM), the beam ellipticity (e), and the beam orientation (ψ_{ell}). Moreover, this fit has been used to define the beam center so that the beam pointing directions agree with the convention adopted in Planck Collaboration II (2013). The fit is performed in the plane of the *Planck* field of view, centred along the nominal line of sight (LOS) defined in Tauber et al. (2010). In Fig. 2 the LFI footprint on the sky is reported for both polarization arms. The data selection is done using the pointing information contained in the satellite Attitude History File (Planck Collaboration II 2013), which in turn is used to infer the nominal LOS direction synchronously with the sampled data. The data selected for fits to Jupiter lie on square grids centred with respect to the main beam pointing direction, of about 1.7° in total size at 70 GHz, 2.6° at 44 GHz, and 3.8° at 30 GHz.

For each radiometer arm, the selected data are characterized by an array of data samples specified by the signal amplitude (in thermodynamic temperature) during the transit, the positions (x, corresponding to the scan circles, and y, corresponding to the positions along each scan circle) of Jupiter during the transit, and the distances between *Planck* and the planet itself during the transit. An initial guess for the main beam input parameters and their possible ranges has been evaluated directly on the measured timelines, together with an estimate of the noise corresponding to the sensitivity of the ensemble of signal data. Since the noise level has an average value far from zero, an offset has been applied in order to have a noise characterized by a null average value. Furthermore, only the data with a signal above the 3σ level from the noise have been considered in the minimisation routine of the fitting code. This implies slightly higher error bars, but guarantees a negligible effect due to the background. No destriping was performed on the timelines because it was found that the $1/f$ noise does not affect the reconstructed beam shape above –20 dB. In particular, the $1/f$ noise will not affect our later estimate of the window functions because these are obtained from simulated beams derived from a tuned optical model, as described later in this section. The fit procedure gives an analytical description of the LFI beams, through the parameters that characterize the elliptical Gaussian profile and the corresponding statistical uncertainties; the latter are computed using the Minuit processor `MINOS`[2] which calculates the parameter errors by taking into account both parameter correlations and non-linearities.

Table 2 reports the main beam descriptive parameters with the estimated uncertainties evaluated from the stacked beams obtained from the four Jupiter transits. In the bar charts, shown in Figs. 3 and 4, the four transits are considered separately and then stacked[3]. It is evident that the four measurements give basically the same results. Thus, no optical ageing effects are evident in these data, which were taken from October 2009 to August 2011.

[2] `http://seal.web.cern.ch`

[3] FWHM = $\sqrt{8\times\log_{10}(2)\times\sigma^b_{max}\times\sigma^b_{min}}$; $e = \sigma^b_{max}/\sigma^b_{min}$; ψ_{ell} is defined as the angle between the major axis of the ellipse and the x-axis of the LOS frame.

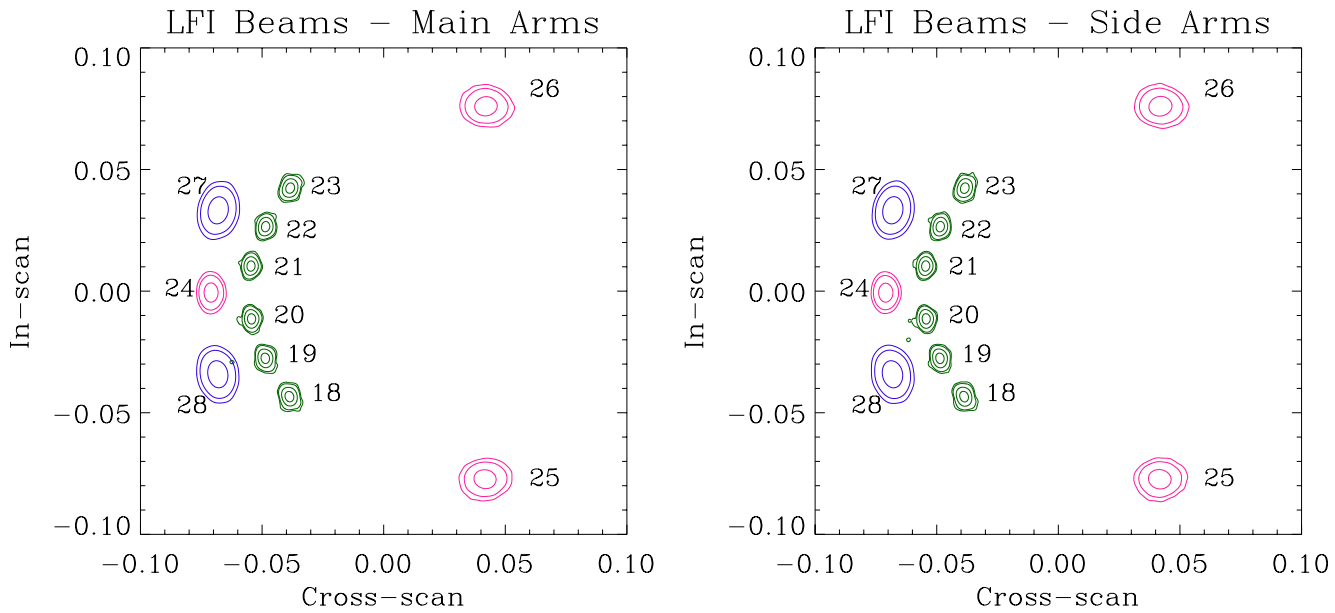

Fig. 2. Scanning beam profiles for both polarization arms, reconstructed from the first four Jupiter transits. The beams are plotted in contours of –3, –10, –20, and –25 dB from the peak at 70 GHz (green), and –3, –10, –20 at 30 (blue) and 44 GHz (pink).

The improvement in terms of the uncertainties obtained using the four scans together is remarkable.

Table 2. Main beam descriptive parameters of the scanning beams, with uncertainties ($1\,\sigma$).

Beam	FWHM (arcmin)	Ellipticity	$\psi_{\rm ell}$ (degrees)
70 GHz			
18M	13.41 ± 0.03	1.24 ± 0.01	85.51 ± 0.68
18S	13.47 ± 0.03	1.28 ± 0.01	86.35 ± 0.55
19M	13.14 ± 0.04	1.25 ± 0.01	78.94 ± 0.67
19S	13.09 ± 0.03	1.28 ± 0.01	79.12 ± 0.58
20M	12.84 ± 0.03	1.27 ± 0.01	71.62 ± 0.62
20S	12.84 ± 0.04	1.29 ± 0.01	72.61 ± 0.61
21M	12.76 ± 0.03	1.28 ± 0.01	108.00 ± 0.52
21S	12.87 ± 0.03	1.29 ± 0.01	106.98 ± 0.57
22M	12.92 ± 0.03	1.27 ± 0.01	102.05 ± 0.57
22S	12.98 ± 0.03	1.28 ± 0.01	101.74 ± 0.57
23M	13.33 ± 0.03	1.24 ± 0.01	93.48 ± 0.67
23S	13.33 ± 0.04	1.28 ± 0.01	93.60 ± 0.59
44 GHz			
24M	23.23 ± 0.07	1.39 ± 0.01	89.85 ± 0.53
24S	23.10 ± 0.07	1.34 ± 0.01	89.98 ± 0.53
25M	30.28 ± 0.10	1.19 ± 0.01	115.41 ± 1.02
25S	30.92 ± 0.10	1.19 ± 0.01	117.34 ± 1.02
26M	30.37 ± 0.12	1.20 ± 0.01	62.13 ± 1.14
26S	30.61 ± 0.11	1.19 ± 0.01	61.42 ± 1.09
30 GHz			
27M	33.06 ± 0.10	1.37 ± 0.01	101.24 ± 0.53
27S	33.12 ± 0.11	1.38 ± 0.01	101.37 ± 0.54
28M	33.17 ± 0.11	1.37 ± 0.01	78.53 ± 0.57
28S	33.28 ± 0.10	1.36 ± 0.01	78.87 ± 0.54

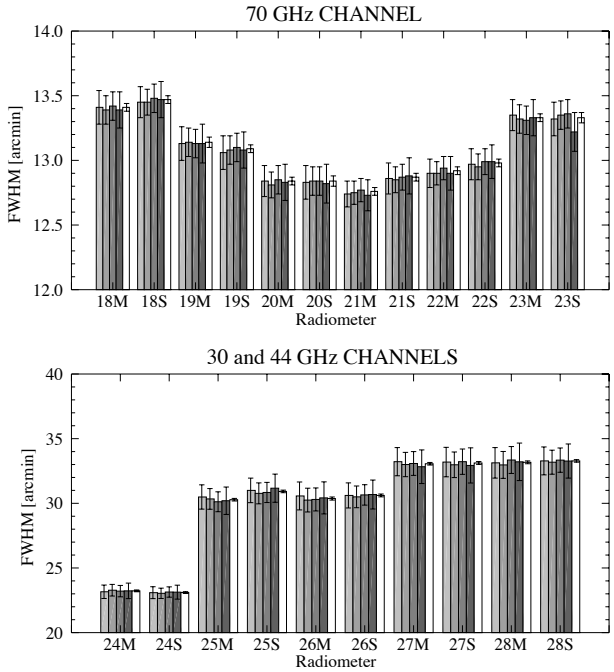

Fig. 3. FWHM at 70 GHz (upper panel) and 30/44 GHz (lower panel) for the four Jupiter scans (grey bars) and for the stacked beams (white bar).

2.2. From optical beams to scanning beams

The optical beams are the optical response of the feed horns coupled to the *Planck* telescope. They are independent of both the radiometer response (bandshape and non-linearity) and the satellite motion (spinning and scanning strategy). They represent the pure optical transfer function for *Planck* LFI.

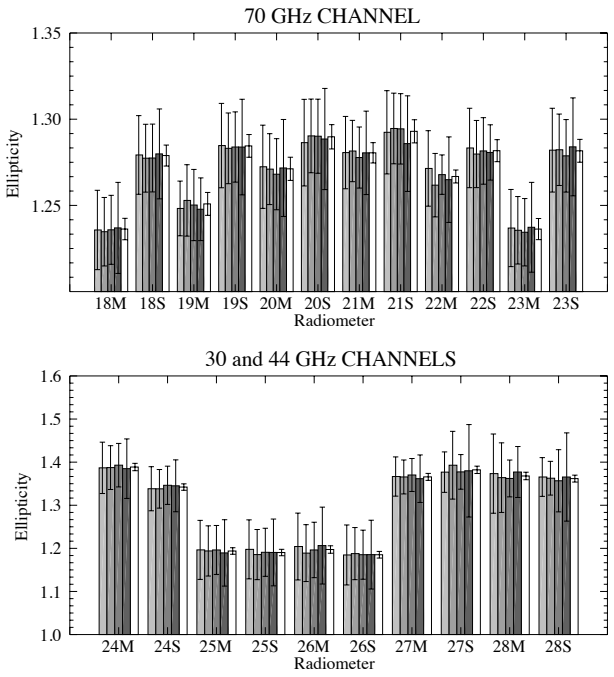

Fig. 4. Ellipticity at 70 GHz (upper panel) and 30/44 GHz (lower panel) for the four Jupiter scans (grey bars) and for the stacked beams (white bar).

2.2.1. Main beams

In the main beam region, the optical beams have been evaluated from simulations carried out by the application of physical optics and the physical theory of diffraction using GRASP[4]. A dedicated optical study has been carried out with the goal of fitting the simulated beams to the in-flight measurements. The optical model was tuned to minimize the binned residual maps down to –15 dB from the power peak, as described in (Planck Collaboration ES 2013). This approach is preferable to using polynomial fits because it is less affected by the noise and the background: the optical model is much more rigid than polynomial fits, and the full focal plane is simultaneously fitted with a single optical model. The reason for this study is to produce an ensemble of noise-free beams that are representative of the *Planck* LFI flight optical beams, and also both account for beam aberrations at very low levels and include the cross-polarization response, which was not measured in flight. Of course, before the comparison with the data, the optical beams are properly smeared to take into account the satellite motion. Beam smearing comes from the fact that, while integrating toward a particular direction in the sky, the satellite moves and the optical beam is convolved with a top hat along the scanning direction. Since during the scanning the beam moves rigidly, the convolution is equivalent to an average. Whereas this effect is negligible in the calibration step (Planck Collaboration V 2013), this is not the case for the main beam measurements with planets, for which this effect smears the optical beam along the scan direction, increasing the beam asymmetries in a non-negligible way.

In Fig. 5 the maps obtained from the difference between measurements and simulations for the 70 GHz beams are shown; the same comparison has been plotted for the 44 GHz radiometers in Fig. 6, and for the 30 GHz radiometers in Fig. 7. The colour scale is 2.25 times the rms of the beam difference and the units of the color bar are in thousandths of the peak height, i.e., 0.1% of the beam maximum. The colour scale has been symmetrized around in the minimum and maximum values so that the zero level is green in all the plots. The size of each patch is fixed: 120'×120' for 30 and 44 GHz and 50'×50' for 70 GHz.

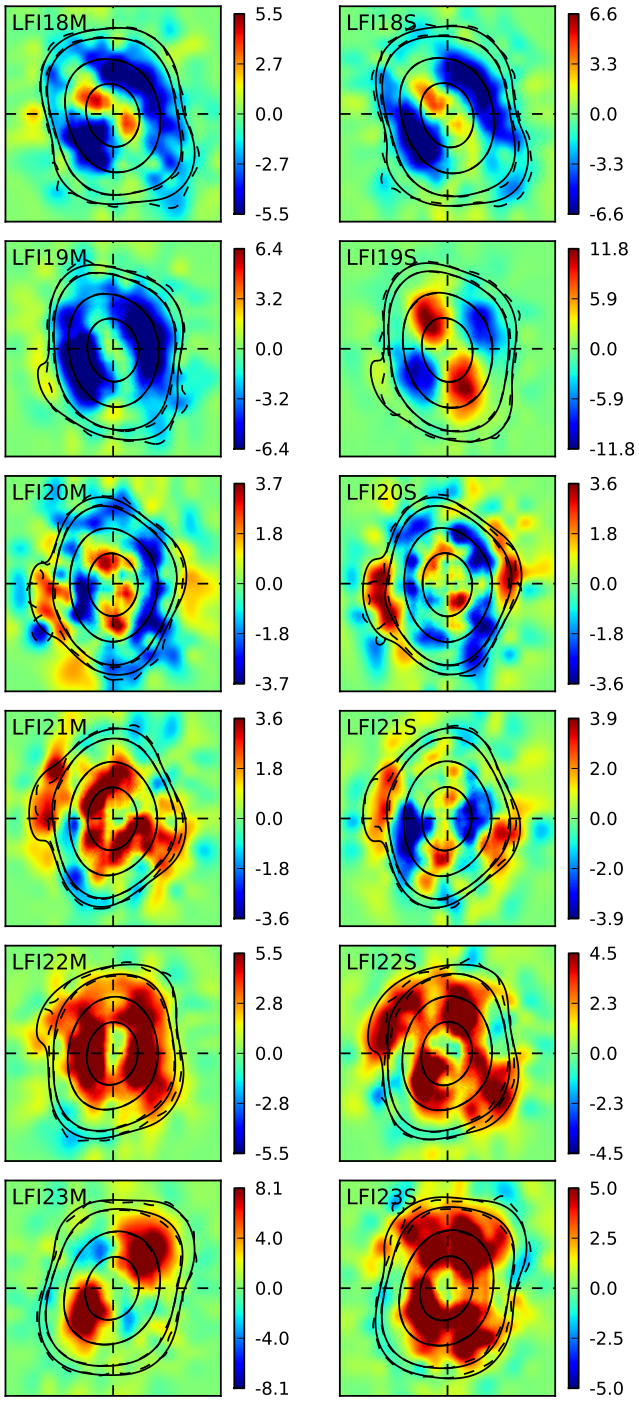

Fig. 5. Difference between measured (dashed line) scanning beams and simulated (solid line) beams (70 GHz channel). The colour scale is 2.25 times the rms of the beam difference and the units of the colour bar are in thousandths of the peak height, i.e., 0.1% of the beam maximum. The contours correspond to –3, –10, –20, and –25 dB from the peak. The size of each patch is 50'×50', centred along the beam line of sight.

[4] The GRASP software was developed by TICRA (Copenhagen, DK) for analysing general reflector antennas (http://www.ticra.it).

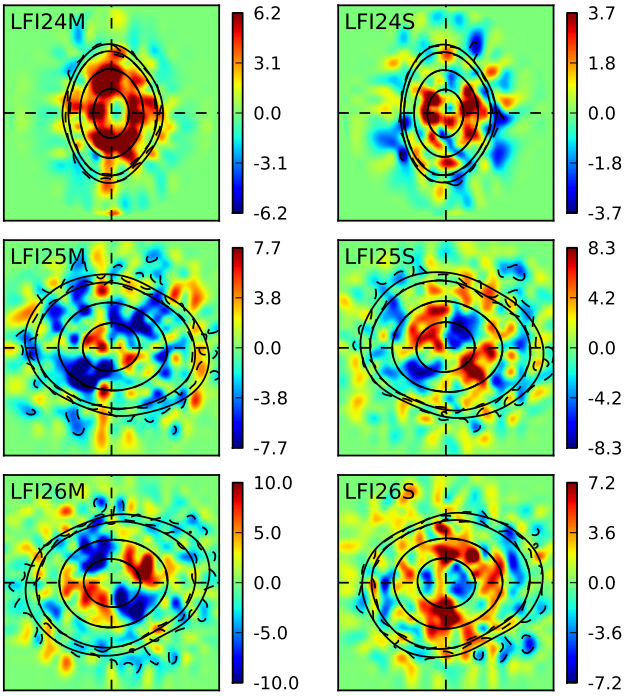

Fig. 6. Difference between measured (dashed line) scanning beams and simulated (solid line) beams (44 GHz channel). The colour scale is 2.25 times the rms of the beam difference and the units of the colour bar are in thousandths of the peak height, i.e., 0.1% of the beam maximum. The contours correspond to –3, –10, –20, and –25 dB from the peak. The size of each patch is 120'×120', centred along the beam line of sight.

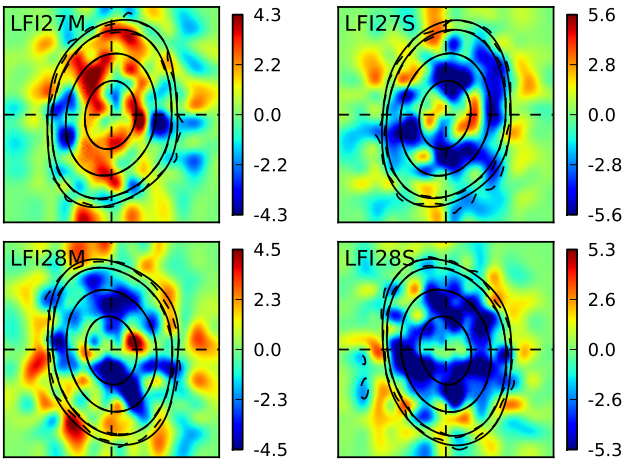

Fig. 7. Difference between measured (dashed line) scanning beams and simulated (solid line) beams (30 GHz channel). The colour scale is 2.25 times the rms of the beam difference and the units of the colour bar are in thousandths of the peak height, i.e., 0.1% of the beam maximum. The contours correspond to –3, –10, –20, and –25 dB from the peak. The size of each patch is 120'×120', centred along the beam line of sight.

Table 3 reports the main beam efficiency of each LFI optical beam, together with the solid angles. The main beam efficiency is defined as:

$$\eta = \frac{\Omega_{\rm MB}}{4\pi} \tag{3}$$

where $\Omega_{\rm MB}$ is the main beam solid angle calculated with the pattern normalized to the isotropic level. In the same Table are also reported the main beam solid angles of the simulated and scanning beams; the values agree to better than 1%.

Table 3. Beam efficiency and solid angles computed on the optical beams and simulated beams. In the first column the main beam efficiency, η, derived from optical beams, is reported. In the second column we report the percentage of the power entering the sidelobes ($f_{\rm sl}$): these values are directly computed as $1-\eta$. In the last column the solid angles computed on the scanning beams are reported. The $1\,\sigma$ statistical error on the estimated solid angle from the scanning beams is about 0.2%. The comparison between the simulated beams and the scanning beams shows that most of the solid angles agree to better than 1%. The averaged values of the simulated beams are 194, 850, and 1183 arcmin^2 at 70, 44, and 30 GHz, respectively. The averaged values of the measured scanning beams are 193, 849, and 1182 arcmin^2 at 70, 44, and 30 GHz, respectively.

Beam	η (%)	$f_{\rm sl}$ (%)	$\Omega_{\rm opt}$ (arcmin^2)	$\Omega_{\rm sim}$ (arcmin^2)	$\Omega_{\rm scn}$ (arcmin^2)
70 GHz					
18S	99.34	0.66	198.10	203.28	205.81
18M	99.42	0.58	196.89	201.84	203.98
19S	99.29	0.71	188.65	193.34	193.51
19M	99.35	0.65	148.23	191.60	195.04
20S	99.18	0.82	181.21	185.63	185.51
20M	99.21	0.79	180.43	185.20	185.45
21S	99.20	0.80	182.50	186.94	186.63
21M	99.21	0.79	181.26	185.71	183.87
22S	99.27	0.73	188.18	193.07	190.22
22M	99.34	0.66	187.45	192.07	188.24
23S	99.35	0.65	199.95	204.84	200.91
23M	99.43	0.57	198.74	203.72	200.99
44 GHz					
24S	99.84	0.16	576.85	590.99	591.86
24M	99.79	0.21	589.99	602.42	594.76
25S	99.80	0.20	1020.68	1041.63	1040.47
25M	99.79	0.21	967.93	990.28	996.72
26S	99.80	0.20	1006.67	1027.13	1019.03
26M	99.79	0.21	967.93	989.89	993.56
30 GHz					
27S	99.33	0.67	1153.02	1181.94	1184.64
27M	99.30	0.70	1158.00	1186.14	1174.48
28S	99.34	0.66	1153.14	1180.99	1188.41
28M	99.29	0.71	1152.56	1181.98	1179.34

2.2.2. Beam validation through deconvolution

To test the goodness of the beam representation, the maps for each individual horn at 30 GHz and 44 GHz have been deconvolved using the `ArtDeco` beam deconvolution algorithm described in Keihanen & Reinecke (2012). The code takes as input the time-ordered data stream, along with pointing information and the harmonic representation of the simulated beam, to construct the harmonic a_{slm} coefficients that represent the sky signal. From the harmonic coefficients we further construct a sky map,

which is now free from the effects of beam asymmetry, assuming that our beam representation is correct.

Before deconvolution we ran the time-ordered data through the Madam map-making code (Keihänen et al. 2010), to remove low-frequency noise. We saved the baselines that represent the correlated noise component, and subtracted them from the original data stream. The cleaned data thus consist of signal with a residual noise component that is dominated by white noise. This was then used as input to the deconvolution code.

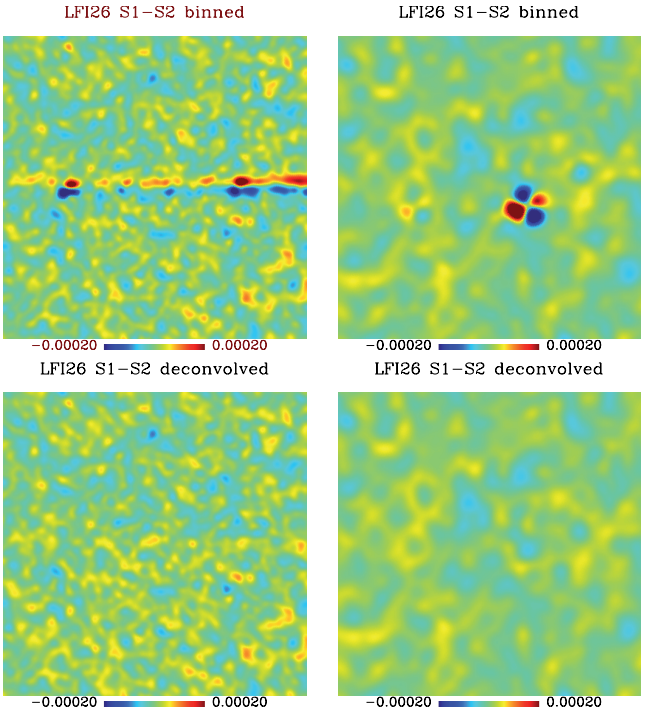

Fig. 8. Comparison between survey differences of binned and deconvolved maps obtained using the simulated beam, LFI26. The maps were smoothed to 1° resolution in order to suppress noise, and the units are Kelvin. The first row of each image corresponds to the binned map, showing a zoom into the Galactic region slightly left from the centre (left), and into an unidentified point source at location (–90°,0°) (right). The improvement in the deconvolved images is clear.

We have run the deconvolution on data from each single survey, and looked for residual differences between single-survey maps. Results for horn LFI26 are shown in Fig. 8, where the difference between first "S1" and second "S2" survey maps is reported. The left-hand column shows a zoom into the Galactic region at location (–40°,0°). One image covers a square of width 13.3°. The right-hand column shows a zoom into a point source near location (–90°,0°). The width of this image is 16.7°. In the absence of beam asymmetry and other systematics, the difference should be due to noise only.

The top row shows, for comparison, the difference between binned maps. In this case, the maps were binned directly from the time-ordered data, without attempting to correct for beam effects. A given region on the sky is scanned with different beam orientations during the different surveys. This gives rise to the residual signal that is evident in the top row images.

The maps were smoothed to a 1° (FWHM) resolution, in order to suppress noise. In the case of binned maps this was achieved by smoothing with a symmetric Gaussian beam with FWHM of 50'. Combined with the width of the radiometer beam, this gives a total smoothing of approximately 1°.

The bottom row shows the corresponding difference of the deconvolved maps. We show the same regions as in the top row and with the same scaling. We smoothed the deconvolved harmonic coefficients with a 1° (FWHM) Gaussian beam, and constructed a sky map through harmonic expansion. Deconvolution almost completely removes the Galactic residual, as well as the "butterfly" pattern of the point source. This indicates that the simulated beams, based on the tuned optical model, are a good representation of the true beams.

The deconvolution is not part of the nominal pipeline but this test provides an important cross-check on the beam representation since it tests the beam model against the data in a way that is independent from the construction of the model.

2.2.3. Spectral dependence of beam geometry

Throughout this work, we have assumed a monochromatic response at each LFI frequency. In fact, the bandpasses are wide, and vary in detail from one radiometer to another, even within the same band. The effective centre frequency for each band used in this paper was calculated assuming a thermal (CMB) spectrum. For different source spectra, the central frequency shifts. We must also take account of the fact that the beam pattern has some frequency dependence. The geometry of the beams is characterized by three parameters described in the previous section: the FWHM; the ellipticity; and the orientation of the beam $\psi_{\rm ell}$. We have investigated the effect on the LFI beams of assuming a power-law spectrum with power index α ranging from −6 to +6, where $\alpha = 2$ is representative of the CMB spectrum and $\alpha = 0$ of a flat spectrum. We start by generating GRASP models of the main beam $B_\nu(\boldsymbol{n})$ at a set of frequencies defined by splitting the bandpass into 15 equally spaced steps centred on the nominal central band frequency. The 15 beam maps were then averaged by weighting each GRASP map pixel by the bandpass $\tau(\nu)$ and the source spectrum ν^α, giving the effective beam pattern

$$\bar{B}_\alpha(\boldsymbol{n}) = N^{-1} \int d\nu\, \tau(\nu)\nu^\alpha B_\nu(\boldsymbol{n}), \qquad (4)$$

with $N = \int d\nu\, \tau(\nu)\nu^\alpha$. We then derived the geometric beam parameters as a function of α. Since the telescope is achromatic, only slight variations of the geometric beam parameters are observed. In addition, the bandpass averaging process further reduces the variability with respect to the monochromatic case. The most interesting result is that the three geometrical parameters vary nearly linearly with α, with different slopes for each radiometer. The most sensitive radiometer in FWHM is LFI28-S, which had $d\mathrm{FWHM}/d\alpha$ of about to 3×10^{-4} degrees. Changing α from +2 to −2 will cause a relative change of at most 0.2%, 0.3% and 0.4% respectively in the FWHM at 30, 44, and 70 GHz, well below the 1% level. A similar range of relative variations occurs for the beam ellipticity. For the orientation parameter, $\psi_{\rm ell}$, the amplitude of $d\psi_{\rm ell}/d\alpha$ varies from a minimum value of -2×10^{-4} degrees (for the detector LFI24-S) to a maximum of 0.36 degrees (for LFI26-M), so that a change in the spectral index α from −2 to +2 will produce a rotation of the beam of 1.4 degrees at most, in one direction or the other. Those values (assuming a CMB spectrum) contribute to the overall calibration uncertainty (Planck Collaboration V 2013), and we emphasise that these uncertainties in the beam properties are completely independent of the colour corrections needed to adjust intensity scales for sources with non-thermal spectra.

2.2.4. Sidelobes

The response of the beam pattern outside the main beam needs to be carefully understood, as it may have significant impact on the *Planck* data analysis. Although a full physical optics computation could be developed to predict accurately the antenna pattern of the telescope, this is not the case for the whole-spacecraft simulations since the physical optics approach cannot be easily applied when multiple diffractions and reflections between scattering surfaces are involved. For this reason, we have calculated the sidelobe patterns through the GRASP multi-reflector geometrical theory of diffraction (MrGTD), which computes the scattered field from the reflectors by performing backward ray tracing. This represents a suitable method for predicting the full-sky radiation pattern of complex mm-wavelength optical systems in a reasonable time. The MrGTD sequentially computes the diffraction fields from any reflector surfaces that are illuminated, starting from the feed horn. The sequence of scatterers and the type of interaction (reflection or diffraction, occurring on each scatter) must be defined in the input to the simulation. The simplest (first order) optical contributions producing significant power levels are reflections onto the sub-reflector, onto the main reflector, and onto the baffle, as well as diffractions by the sub-reflector, by the main reflector, and by the baffle. Other non-negligible contributions derive from two interactions with the reflectors (second order – for example, rays reflected on the sub-reflector and then diffracted by the main reflector), three interactions (third order – for example, rays reflected on the sub-reflector, diffracted by the main reflector, and then diffracted by the baffle) and so on. Although MrGTD is, in general, less time consuming than a full physical optics calculation, it should be applied in a rigorous way in order to obtain reliable results, especially at low power levels (down to –50 dBi). In addition, when many scattering surfaces are involved, the number of ray tracing needed may lead to unacceptable computational time, even with MrGTD. Since our analysis requires the production of band-integrated patterns to account for the frequency-dependent beam responses and the radiometer bandpasses, for now the sidelobes simulations have been carried out only up to the first order plus two contributions at the second order (reflections and diffractions on the sub-reflector, and then diffracted by the main reflector).

We found that the beam solid angle in the simulated sidelobe region is about a factor two lower than the expected value (see $f_{\rm sl}$ reported in Table 3). It is evident that the first order approximation adopted underestimates the actual integrated power in the sidelobes. Consequently, the sidelobes model must take into account the impact of higher-order contributions combined with physical optics analyses. We will do so in the future.

Careful analysis of the LFI 30 GHz data has revealed the imprint of Galactic radiation received through the far sidelobes. Such a detection is amplified when taking the difference between maps of even and odd surveys, because, due to the different satellite orientation, the coupling between the sidelobe pattern and Galactic radiation is reversed. A detailed discussion of the systematic effects introduced by sidelobe pickup at 30 GHz is given in Planck Collaboration III (2013). The expectations of the sidelobe pick-up based on the known level of Galactic emission (as measured by *Planck* itself) and our sidelobe model, are in good agreement in morphology with the observed effect, as shown in Fig. 9. The residual ring clearly visible in the third panel of Fig. 9 is in agreement with the previous conclusion that the sidelobe model should be improved by adding higher order contributions, possibly combined with full physical optics analyses. In the bottom panel of the Fig. 9 we show the difference between data and the simulations, these being amplified by a factor equal to the ratio of the power entering the sidelobes (computed from the main beam efficiency) and the integral of the simulated sidelobes. It is evident that, once we have re-normalised the sidelobe amplitude, the ring artifact almost completely disappears.

It should be noted that, while the sidelobe effect introduces additional complication in the analysis, its detection at 30 GHz provides an important validation of the simulated beams, which can be trusted even to very low power levels in the higher-frequency *Planck* cosmological channels as well, for which the sidelobes signatures are not measurable. This has important consequences for our future analysis aimed at CMB polarization. Our plan is to produce refined in-band integrated beams for each radiometer, to be included into the polarization data analysis pipeline.

3. Effective Beams

The effective beam is the average of all scanning beams that cross a given pixel of the sky map, given *Plancks* scan strategy. The effective beams capture the complete information about the difference between the true and observed images of the sky. They are, by definition, the objects whose convolution with the true CMB sky produce the observed sky map. Similarly, the effective beam window functions capture the difference between the true and observed angular power spectra of the sky. We compute the effective beam at each sky pixel for each LFI frequency scanning beam and scan history using the FEBeCoP (Mitra et al. 2011) method, as was done in *Planck*'s early release (Planck HFI Core Team 2011b).

The pre-computation of the effective beams was executed at the National Energy Research Scientific Computing Center (NERSC) in Berkeley (California). The beam data were delivered to the *Planck* data processing centres (Planck Collaboration II 2013; Planck Collaboration VI 2013) over the network, on tape and disk, and ingested into the Data Management Component (DMC). FEBeCoP associated application software was developed and installed to use the effective beams, e.g., fast Monte Carlo full sky convolution codes.

In estimating the effective beams, a cut-off is applied to the input simulated beams. From several tests performed we converged to a cut-off radius of 2.5 × FWHM. The beam efficiency of the simulated beams within this cut-off radius is reported in Table 4.

For a detailed account of the algebra involving the effective beams for temperature and polarization see Mitra et al. (2011). Here we summarize the main results.

The observed temperature sky $\widetilde{\boldsymbol{T}}$ is a convolution of the true sky $\boldsymbol{T}$ and the effective beam $\boldsymbol{B}$,

$$\widetilde{\boldsymbol{T}} \;=\; \Delta\Omega\, \boldsymbol{B} \cdot \boldsymbol{T}, \tag{5}$$

where the effective beam can be written for the temperature in terms of the pointing matrix A_{ti} and the scanning beam $b(\hat{\boldsymbol{r}}_j, \hat{\boldsymbol{p}}_t)$ as

$$B_{ij} \;=\; \frac{\sum_t \mathsf{A}_{ti}\, b(\hat{\boldsymbol{r}}_j, \hat{\boldsymbol{p}}_t)}{\sum_t \mathsf{A}_{ti}}\,. \tag{6}$$

Here t represents time samples, A_{ti} is 1 if the pointing direction falls in pixel number i, else it is 0; $\boldsymbol{p}_t$ represents the exact pointing direction (not approximated by the pixel centre location), and $\hat{\boldsymbol{r}}_j$ is the centre of pixel number j, where the scanning beam $b(\hat{\boldsymbol{r}}_j, \hat{\boldsymbol{p}}_t)$ is being evaluated (if the pointing direction

Table 4. Main beam efficiencies computed on the simulated beams using a cut-off radius of 2.5 FWHM: main and side arm efficiencies are reported in the first two columns, the average value of the two arms is reported in the third column, and the difference between the two arms is reported in the last column.

Horn	Main	Side	Mean	(Diff)
70 GHz				
LFI-18	0.99345	0.99262	0.99304	–0.00082
LFI-19	0.99270	0.99206	0.99238	–0.00065
LFI-20	0.99111	0.99084	0.99098	–0.00027
LFI-21	0.99115	0.99105	0.99110	–0.00010
LFI-22	0.99259	0.99184	0.99222	–0.00075
LFI-23	0.99360	0.99274	0.99317	–0.00086
44 GHz				
LFI-24	0.99762	0.99826	0.99794	0.00064
LFI-25	0.99788	0.99792	0.99790	0.00005
LFI-26	0.99787	0.99793	0.99790	0.00006
30 GHz				
LFI-27	0.99247	0.99282	0.99264	0.00036
LFI-28	0.99230	0.99284	0.99257	0.00054

falls within the cut-off radius of 2.5 × FWHM, for LFI channels). An analogous formula can be written for the temperature + polarization effective beam, including the weight vector $\boldsymbol{w}_t \equiv [1, \gamma\cos(2\psi), \gamma\sin(2\psi)]$, as:

$$B_{ij} = \left[\sum_t \mathsf{A}_{ti}\boldsymbol{w}_t\boldsymbol{w}_t^{\mathrm{T}}\right]^{-1} \sum_t \mathsf{A}_{ti} b(\hat{r}_j, \hat{p}_t)\boldsymbol{w}_t\boldsymbol{w}_t^{\mathrm{T}}. \quad (7)$$

As an example, in Figs. 11, 12, and 13 we compare images of four sources (assumed to be unresolved) from the *Planck* Early Release Compact Source Catalogue (ERCSC) (Planck Collaboration VII 2011) and FEBeCoP point spread functions (i.e., the transpose of the effective beam matrix) on the same patch of the sky for the LFI channel maps. The galactic coordinates (l, b) of the four sources are shown under the colour bar: in our sample, these are, respectively, (305.1°, 57.1°), (86.1°, –38.2°), (290.0°, 64.4°) and (184.5°, –5.8°), from left to right in the three figures.

We further performed a 2D Gaussian fit of the effective beam at several positions of the sky and studied the distribution of the fitted parameters: beam FWHM; ellipticity; solid angle; and orientation with respect to the local meridian. In order to perform such statistics, we sampled the sky (fairly sparsely) at 768 directions which were chosen as HEALpix (Górski et al. 2005) N_{side}=8 pixel centres to uniformly sample the sky. The histograms of these quantities are shown in Fig. 14. From the histograms, we derive the statistical properties of these quantities (mean values and standard deviations), which are provided in Table 5).

In Fig. 10 we show the sky variation of ellipticity, FWHM (relative variation with respect to the FWHM of the scanning main beam), psi (orientation of the effective beam) and beam solid angle (relative variation with respect to the scanning main beam solid angle reported in Table 2) of the best-fit Gaussian to the effective beam at HEALpix N_{side}=16 pixel centres for 70 GHz. The effective beam is less elliptical near the ecliptic poles, where more scanning angles symmetrize the beam.

The main beam solid angle of the effective beam, Ω_{eff}, is estimated according to the definition: $4\pi\sum(B_{ij})/\max(B_{ij})$, i.e., as an integral over the full extent of the effective beam. From the effective beam solid angle we can estimate the effective FWHM, under a Gaussian approximation: these are tabulated in Table 5. The reported $\mathrm{FWHM}_{\mathrm{eff}}$ are derived from the solid angles, under a Gaussian approximation. The mean(FWHM) are the averages of the Gaussian fits to the effective beam maps. The former is best used for flux determination, the latter for source identification.

Note that the FWHM and ellipticity in Table 5 differ slightly from the values reported in Table 2; this results from the different way in which the Gaussian fit was applied. The scanning beam fit was determined by fitting the profile of Jupiter on timelines and limiting the fit to the data with a signal above the 3σ level from the noise, while the fit of the effective beam was computed on the maps of the simulated beams projected in several position of the sky; the latter are less affected by the noise.

In Table 6 we indicate with $\Omega_{\mathrm{eff}}^{(1)}$ the beam solid angle estimated up to a radius equal to the $\mathrm{FWHM}_{\mathrm{eff}}$ (as defined above), while $\Omega_{\mathrm{eff}}^{(2)}$ indicates the beam solid angle estimated up to a radius equal to twice the effective FWHM ($\mathrm{FWHM}_{\mathrm{eff}}$). These were estimated according to the procedure followed in the aperture photometry code for the *Planck* Catalog of Compact Sources (PCCS) (i.e., if the pixel centre does not lie within the given radius it is not included). These additional quantities were evaluated for the production of the PCCS (Planck Collaboration XXVIII 2013).

4. Beam Window Function

CMB temperature anisotropies are a scalar random field on a sphere, and can be decomposed in spherical harmonic coefficients:

$$a_{\ell m} = \int d\Omega T(\hat{n}) Y^*_{\ell m}(\hat{n}), \quad T(\hat{n}) = \sum_{\ell m} a_{\ell m} Y_{\ell m}, \quad (8)$$

where

$$\langle a_{\ell m}\rangle = 0, \quad \langle a_{\ell m} a^*_{\ell' m'}\rangle = \delta_{\ell\ell'}\delta_{mm'} C_\ell. \quad (9)$$

The finite angular resolution of an instrument $b(\hat{n}, \hat{n}')$ can be described through a convolution in real space:

$$T_{\mathrm{obs}}(\hat{n}) = \int d\Omega b(\hat{n}, \hat{n}') T(\hat{n}'), \quad (10)$$

which is equivalent to a low-pass filter in harmonic space, and whose effective action on the power spectrum can be written as:

$$C_\ell^{\mathrm{obs}} = W_\ell C_\ell, \quad (11)$$

where W_ℓ is the beam window function.

As discussed in the previous section, a basic symmetric Gaussian approximation is not a good description of *Planck* effective beams. Moreover, the combination of intrinsic beam asymmetry and scanning strategy produces effective beams that vary significantly over the sky. Therefore, in order to produce accurate estimates of the beam window functions, we are forced to use detailed Monte Carlo simulations. This has been implemented using two approaches: first, full timeline-to-map simulations, where the CMB signal is convolved with realistic scanning beams in harmonic space, and then projected into a TOD through the *Planck* scanning strategy and processed in the same way as real data; and second, pixel space convolution of CMB signal only maps using the effective beams derived with FEBeCoP.

In principle, for full-sky maps the effective azimuthally averaged beam window function can be estimated directly from Eq. 11:

$$W_\ell = \langle C_\ell^{\mathrm{obs}}\rangle / C_\ell, \quad (12)$$

Table 5. Mean and standard deviation of FWHM, ellipticity, orientation, and solid angle of the FEBeCoP effective beams computed with the simulated beams. $\mathrm{FWHM_{eff}}$ is the effective FWHM estimated from the main beam solid angle of the effective beam, $\Omega_{\mathrm{eff}} = \mathrm{mean}(\Omega)$, under a Gaussian approximation.

Channel	mean(FWHM) (arcmin)	σ(FWHM) (arcmin)	mean(e)	$\sigma(e)$	mean(ψ) (deg)	$\sigma(\psi)$ (deg)	mean(Ω) (arcmin^2)	$\sigma(\Omega)$ (arcmin^2)	$\mathrm{FWHM_{eff}}$ (arcmin)
70	13.252	0.033	1.223	0.026	0.587	55.066	200.742	1.027	13.31
44	27.005	0.552	1.034	0.033	0.059	53.767	832.946	31.774	27.12
30	32.239	0.013	1.320	0.031	–0.304	55.349	1189.513	0.842	32.34

Table 6. Band averaged beam solid angles.

Channel	Ω_{eff} (arcmin^2)	spatial var. (arcmin^2)	$\Omega^{(1)}_{\mathrm{eff}}$ (arcmin^2)	spatial var. (arcmin^2)	$\Omega^{(2)}_{\mathrm{eff}}$ (arcmin^2)	spatial var. (arcmin^2)
70	200.74	1.03	186.26	2.30	200.59	1.03
44	832.95	31.77	758.68	29.70	832.17	31.81
30	1189.51	0.84	1116.49	2.27	1188.95	0.85

where C_ℓ^{obs} is the power spectrum of simulated CMB-only maps, C_ℓ is the fiducial model used as input, and the ensemble average is taken over the Monte Carlo simulations. However, in a realistic case we mask out some regions of the sky that are contaminated by foreground, and the above equation no longer applies. Instead, using the same notation as in Hivon et al. (2002), we can write:

$$\langle C_\ell^{\mathrm{obs}} \rangle = \sum_{\ell'} M_{\ell\ell'} W_{\ell'} \langle C_{\ell'} \rangle, \tag{13}$$

where the coupling kernel $M_{\ell\ell'}$ encodes the geometric mode-mode coupling effect introduced by masking the sky. However, we have verified that for the Galactic mask used for power spectrum estimation (Planck Collaboration II 2013; Planck Collaboration XV 2013) the differences between full-sky and cut-sky window functions are marginal with respect to the error envelopes discussed in Sect. 5. Therefore, hereafter we'll use full-sky approximation.

4.1. Timeline-to-map Monte Carlo window functions

Signal-only timeline-to-map Monte Carlo (MC) simulations are produced using Level-S (Reinecke et al. 2006) and HEALpix subroutines and the Madam map-maker (Kurki-Suonio et al. 2009; Keihänen et al. 2010) on the *Louhi* supercomputer at *CSC-IT Center for Science* in Finland; see Appendix B for details.

Starting from a fiducial CMB power spectrum we have generated a set of sky $a_{\ell m}$ realizations of this C_ℓ that are convolved with the beam $a_{\ell m}$ obtained from the simulated scanning beams. Note that the main beams do not collect the full power of the signal, since a small part of the signal spills outside the main beam to form sidelobes. In this MC just the main beam up to 4 FWHM was simulated, not the sidelobes, so the calculated signal values were missing that part of the power that goes to the sidelobes. This was taken into account at the map-making stage. Note that the main beam definition used here (4 FWHM) differs from that adopted in the effective beams computation (2.5 FWHM). The consequences are discussed in Sect. 5.

The CMB timelines for each realization were produced according to the detector pointing for each radiometer, and maps were made from these CMB timelines with Madam. The same Madam parameter settings were used as for the flight maps (Zacchei et al. 2011; Planck Collaboration II 2013). The calibration step was not simulated, as the simulated signal was constructed as already calibrated, except for the effect of power lost to the sidelobes. The impact of sidelobes on the calibration of flight data is discussed in Planck Collaboration V (2013), while its effect on the beam window function will be discussed in Sect. 5 of this paper. For the MC, we assumed that the calibration compensates for the missing power in the main beams, according to the discussion in Sect. 2.2 of Planck Collaboration V (2013).

We produced in this way 30 GHz, 44 GHz, and 70 GHz frequency maps, and the "horn-pair" maps for 70 GHz 18/23, 19/22, and 20/21 from the 15.5 month nominal survey. The computational cost of producing one realization of this set was about 2000 CPUh. Given this relatively large computational cost, we have generated only 102 CMB realizations. Although this leaves some residual scatter in the estimated beam window functions especially at low multipoles, these maps have been generated mostly as a consistency check with respect to the FEBeCoP approach as described below, and therefore the number of simulations is adequate for this purpose.

Full-sky, timeline-to-map Monte Carlo based beam window functions are shown in Fig. 15 for 30, 44, and 70 GHz frequency maps. For 70 GHz we also show the beam window functions obtained considering only subsets of detectors, namely LFI18-23, LFI19-22, and LFI20-21.

4.2. FEBeCoP window functions

FEBeCoP beam window functions are shown in Fig. 16 for 30, 44, and 70 GHz frequency maps. For 70 GHz we also show the beam window functions obtained considering only subsets of detectors, namely LFI18-23, LFI19-22, and LFI20-21. These are computed using the effective beams obtained from the simulated scanning beams with a cutoff radius of 2.5 FWHM. The resulting window functions in full sky approximation are obtained by averaging Eq. 12 over 1000 signal only simulations, where every simulated CMB maps is convolved with the effective beams described in Sect. 3.

In Fig. 17 we show a comparison between MC-based and FEBeCoP beam window functions. Although there are some high-ℓ discrepancies at 70 GHz, these are located at $\ell \gtrsim 1300$ where the beam W_ℓs drop below 0.01.

In addition, however, as we will explain in the next section, we should account for the effect of the different choices for the cutoff radius between the two methods. Our FEBeCoP calculations used a 2.5 FWHM cutoff radius for the main beam, while the timeline-to-map, Monte Carlo window functions are derived using a 4 FWHM cutoff. In order to quantify the agreement, we also show in Fig. 17 the $\pm 1\sigma$ error envelopes that will be discussed in the next section. So we can fairly conclude that in the "region of interest" the two methods agree to 1% level. Since the FEBeCoP algorithm is faster than the timeline-to-map Monte Carlo, it allows for a significantly larger number of simulations (1000 vs 102), resulting in a more accurate estimation of the window functions. For the same reason, FEBeCoP also allows to perform a robust error assessment as presented in the next section. Hence, the FEBeCoP window functions will be used for the power spectrum analysis (Planck Collaboration II 2013; Planck Collaboration XV 2013), and will be distributed within the data release.

With FEBeCoP we also estimate the level of contamination of the transfer functions due to a non-uniform sky sampling within the pixels, comparing the ideal HEALpix pixel window function, which is derived under the assumption of uniform coverage, with the true one computed with FEBeCoP. This effect acts as a noise term in the maps and it becomes important only at very high ℓ. An analytic treatment of the contamination on the maps is described in Appendix F of the HFI Beam paper (Planck Collaboration VII 2013). We quote here the level of distortion of the window function: 0.1% at $\ell = 600$ for 30 GHz, 0.4% at $\ell = 800$ for 30 GHz, and 0.5% at $\ell = 1400$ for 70 GHz, in all the cases within the error bars.

5. Error Budget

We discuss here the main sources of uncertainties in the window functions that have proven to be relevant for the LFI.

5.1. Main beam knowledge

The propagation of the uncertainties in the beam knowledge to the window function has been carried out with a dedicated MC pipeline on the *Planck* optics. The tuned optical model (Planck Collaboration ES 2013) was used as the basis to run MC simulations with about 500 realizations of the *Planck* optics. More specifically, the wavefront at the aperture of the telescope has been artificially distorted by adding to the primary reflector randomly-varying amplitude distortions described as modes of Zernike polynomials, up to the fifth order.

The idea behind this assumption is that the true flight beam comes from a true flight field distribution at the telescope aperture that gives the true wavefront. Any small difference between our telescope model and the real one can be mapped by aberrations on the aperture wavefront. For each wavefront we simulated using GRASP the corresponding beam and we selected only the beams with parameters (angular resolution, ellipticity, and beam orientation) in line with those measured in flight within 3σ level. We used the errors in the determination of each parameter reported in Table 2. We repeated this for all the twenty-two LFI beams producing a set of 3036 beams (corresponding to 138 slightly different optical models). In this way we built a set of beams calculated from plausible optical models of the telescope and whose parameters are in agreement with the parameters we measured in flight. Then this set of beams was used as input to FEBeCoP to compute the corresponding window functions.

The three parameters used in the comparison between simulations and measurements (angular resolution, ellipticity, and beam orientation) are strongly correlated and this original method to obtain the errors on the window function using a MC pipeline on the optics takes this correlation properly into account, avoiding unphysical solutions in which no correlation is assumed. In Fig. 18 we show the beam window functions at 70 GGz for all the 138 simulated optical models. Window functions are normalized to the fiducial for the 70 GHz channel.

5.2. Cutoff radius in the main beam computation and impact of sidelobes

The impact of sidelobes on the calibration has been discussed in Planck Collaboration V (2013). The main result for the discussion presented here is that the gain values are unbiased, and this imposes a constraint on the dipole term of the window function, i.e., $W_1 = 1$, which fixes the normalization. In principle, in order to fully account for beam effects in the window function, one should perform a computation of the window function including the full beam pattern, with either FEBeCoP or the timeline-to-map Monte Carlo. However, this would have a huge computational cost making it unfeasible in a Monte Carlo approach. As a result, LFI beam window functions are derived from Monte Carlo simulations including the main beam only, and therefore it is important to assess the effect of neglecting sidelobes.

We have done a preliminary evaluation by using a analytical approach for calculating the window function. In fact, for a given azimuthally symmetric beam profile $b_s(\theta)$, the corresponding ℓ-space function B_ℓ can be computed using the Legendre transform:

$$B_\ell = \Omega_B b_\ell = 2\pi \int dcos(\theta) b_s(\theta) P_\ell(\theta), \qquad (14)$$

and $W_\ell = B_\ell^2$. We have then considered the symmetrized beam profile for LFI18M detector, and we have computed the corresponding B_ℓ cutting the integration at different angles, namely 2.5 FWHM, 4 FWHM, 2°, and 3°, and imposing the normalization constraint at $\ell = 1$. We report in Fig. 19 the relative difference between B_ℓs obtained for the four cutoff values and the one resulting from full integration. As expected, results show a small ℓ-dependent correction affecting mostly the large angular scales. In particular, extending the calculation up to the near sidleobes makes this effect negligible.

As already stated in Sect. 4, the combination of intrinsic asymmetries in the *Planck* beam and scanning strategy forced us to discard a simple beam symmetrization. The same argument applies here, especially considering that near and far sidelobes are even more asymmetric than the main beam. Therefore, we have extended FEBeCoP calculation for the same LFI18M detector to cutoff radii of 4 FWHM and 3° (corresponding to ~ 9 FWHM). In this case we have used the latter window function as a reference to compare with when computing the relative difference. Results are reported in Fig. 20, confirming that similar conclusions can be drawn for a realistic case as well.

A further improvement in the assessment of the sidelobes effect on the window function has been carried out considering the variation across the band of the sidelobes themselves. Whereas the impact of the main beam variation across the band is small, this is not true for the near and far sidelobes. The 4π beams of the radiometer LFI18M (main beam, near and far sidelobes) were computed at about twenty frequencies across the radiometer bandpass and they were averaged taking into account the radiometer bandshape. The resulting averaged beam has been used

to evaluated the impact on the beam window function using the analytical approach described above. The shape of the bias is very close to that reported in Fig. 19 but the amplitude is slightly different with respect to the monochromatic beam. In the error budget we have considered the worst case in order to be conservative as far as possible.

5.3. Total error budget on window functions

Using the set of simulated beam window functions we have also built the covariance matrix $\mathbf{C}$ in ℓ-space computing:

$$\mathbf{C}_{\ell\ell'} = \langle (W_\ell - \langle W_\ell \rangle)(W_{\ell'} - \langle W_{\ell'} \rangle) \rangle \,, \tag{15}$$

where the averaging is performed on the 138 simulations. Then we have decomposed in eigenvalues (Λ_k) and eigenvectors ($\mathbf{V}_k$) the covariance matrix. In Fig. 21 we show the first eigenmodes for the 70 GHz channel. All the error content is substantially encompassed by the first two eigenvalues, that account for cutoff radius and main beam uncertainties respectively. Figures 22 and 23 show the eigenmodes for the 44 and 30 GHz, respectively. The eigenmodes can be used as input of the Markov Chain Beam Randomization (MCBR) marginalization code to account for beam errors in cosmological parameter estimation (Rocha et al. 2010). We apply the MCBR procedure to a simulated 70 GHz dataset and we find that the parameters mostly affected are n_s, $\Omega_b h^2$, $\Omega_c h^2$, and A_s; the increase of the errors can be quantified respectively as 12% of σ for the first and less then 8% of σ for the others.

6. Conclusions

The optics and electronics of the *Planck* detectors, combined with the satellite motion, determine the instrumental angular response to a sky signal. An accurate characterization and a thorough understanding of the LFI beam patterns is the key to determining their imprint on the transfer function from the observed to the true sky anisotropy spectrum. In this paper we discussed the algorithms used to reveal the most significant LFI beam features that impact the exploration of the underlying cosmology. The in-flight assessment of the LFI main beams relied mainly on the measurements performed during Jupiter crossings. The calibrated data from four Jupiter scans were used to determine the so called *scanning beams*: the signal-to-noise ratio for this data is such as to make it possible to follow the LFI beams profile down to –20 dB from the peak, corresponding to distances from the beam line of sight of about 1.25 FWHM, i.e., the inner parts of the main beams. Fitting the main beam shapes with an elliptical Gaussian, we could express the uncertainties of the measured scanning beam in terms of statistical errors for the Gaussian parameters: ellipticity; orientation; and FWHM. While this method allows the accurate in-flight measurement of the LFI main beams, the (lower) angular response at larger distances from the beam centroid (near and far sidelobes) cannot be directly measured from a single point source signal, mostly because of the noise and background dominance, so it must be modelled differently. Therefore, a further step has been taken to build an optimal model for the full LFI beams profile. We developed a tuned optical model such that the simulated beams would provide the best fit to the available measurements of the LFI main beams from Jupiter: we found that this model represents all the LFI beams with an accuracy of 1%, which has been considered in the propagation of the uncertainties at the window function level. The corresponding simulated sidelobes are, in turn, consistent with the effect induced by the Galactic spillover as observed in survey maps differences. This model, together with the pointing information derived from the focal plane geometry reconstruction (Planck Collaboration II 2013), gives the most advanced and precise noise-free representation of the LFI beams. These were also independently cross-checked through a beam deconvolution test. The simulated beams were the input to calculate the effective beams, which take into account the specific scanning strategy to include any smearing and orientation effects on the beams themselves. The approach was validated by comparing the effective beam Point Spread Functions with images from the Planck Catalogue of Compact Sources.

To evaluate the beam window function, we adopted two independent approaches, both based on Monte Carlo simulations. In one case, we convolved a fiducial CMB signal with realistic scanning beams in the harmonic space to generate the corresponding timelines and maps; in the other case, we convolved the fiducial CMB map with effective beams in the pixel space. The two methods agree to 1% level.

To evaluate the error on the resulting window functions, we took into account the fact that they were calculated assuming full-power main beams. Thus, part of the error budget comes from the propagation of the main beam uncertainties throughout the analysis, while another contribution comes from neglecting near and far sidelobes in the Monte Carlo simulation chain. We found that the two error sources have different relevance depending on the angular scale. Ignoring the near and far sidelobes is the dominant error at low multipoles, while the main beam uncertainties dominate the total error budget at $\ell \geq 600$. Representative values of the total error, for scales of cosmological interest, range from 0.3% ($\ell \approx 200$) to about 0.8% ($\ell \approx 1200$). The total uncertainties in the effective beam window functions are: 2% and 1.2% at 30 and 44 GHz, respectively (at $\ell \approx 600$); and 0.7% at 70 GHz at $\ell \approx 1000$.

Acknowledgements. *Planck* is too large a project to allow full acknowledgement of all contributions by individuals, institutions, industries, and funding agencies. The main entities involved in the mission operations are as follows. The European Space Agency (ESA) operates the satellite via its Mission Operations Centre located at ESOC (Darmstadt, Germany) and coordinates scientific operations via the Planck Science Office located at ESAC (Madrid, Spain). Two Consortia, comprising around 50 scientific institutes within Europe, the USA, and Canada, and funded by agencies from the participating countries, developed the scientific instruments LFI and HFI, and continue to operate them via Instrument Operations Teams located in Trieste (Italy) and Orsay (France). The Consortia are also responsible for scientific processing of the acquired data. The Consortia are led by the Principal Investigators: J.L. Puget in France for HFI (funded principally by CNES and CNRS/INSU-IN2P3-INP) and N. Mandolesi in Italy for LFI (funded principally via ASI). NASA US Planck Project, based at JPL and involving scientists at many US institutions, contributes significantly to the efforts of these two Consortia. The author list for this paper has been selected by the Planck Science Team, and is composed of individuals from all of the above entities who have made multi-year contributions to the development of the mission. It does not pretend to be inclusive of all contributions. The *Planck*-LFI project is developed by an International Consortium lead by Italy and involving Canada, Finland, Germany, Norway, Spain, Switzerland, UK, USA. The Italian contribution to *Planck* is supported by the Italian Space Agency (ASI) and INAF. This work was supported by the Academy of Finland grants 253204, 256265, and 257989. This work was granted access to the HPC resources of CSC made available within the Distributed European Computing Initiative by the PRACE-2IP, receiving funding from the European Community's Seventh Framework Programme (FP7/2007-2013) under grant agreement RI-283493. We thank CSC – IT Center for Science Ltd (Finland) for computational resources. We acknowledge financial support provided by the Spanish Ministerio de Ciencia e Innovaciõn through the Plan Nacional del Espacio y Plan Nacional de Astronomia y Astrofisica. We acknowledge the Max Planck Institute for Astrophysics Planck Analysis Centre (MPAC), funded by the Space Agency of the German Aerospace Center (DLR) under grant 50OP0901 with resources of the German Federal Ministry of Economics and Technology, and by the Max Planck Society. This work has made use of the Planck satellite simulation package (Level-S), which is assembled by the Max Planck Institute for Astrophysics

Planck Analysis Centre (MPAC) Reinecke et al. (2006). We acknowledge financial support provided by the National Energy Research Scientific Computing Center, which is supported by the Office of Science of the U.S. Department of Energy under Contract No. DE-AC02-05CH11231. Some of the results in this paper have been derived using the HEALPix package Górski et al. (2005). The development of *Planck* has been supported by: ESA; CNES and CNRS/INSU-IN2P3-INP (France); ASI, CNR, and INAF (Italy); NASA and DoE (USA); STFC and UKSA (UK); CSIC, MICINN, JA and RES (Spain); Tekes, AoF and CSC (Finland); DLR and MPG (Germany); CSA (Canada); DTU Space (Denmark); SER/SSO (Switzerland); RCN (Norway); SFI (Ireland); FCT/MCTES (Portugal); and PRACE (EU). A description of the Planck Collaboration and a list of its members, including the technical or scientific activities in which they have been involved, can be found at `http://www.sciops.esa.int/index.php?project=planck&page=Planck_Collaboration`.

Appendix A: LFI beams notation

In table A.1 we report a selection of the most important symbols used in this paper.

Appendix B: Timeline-to-map Monte Carlo simulations

Signal-only timeline-to-map Monte Carlo (MC) simulations are produced using Level-S (Reinecke et al. 2006) and Healpix (Górski et al. 2005) subroutines, and the `Madam` map-maker (Kurki-Suonio et al. 2009; Keihänen et al. 2010) on the *Louhi* supercomputer at *CSC-IT Center for Science* in Finland.

Starting from a fiducial CMB power spectrum with $\ell_{\rm max}$ = 3000, we used `syn_alm_cxx` to generate a set of sky $a_{\ell m}$ realizations of this C_ℓ. Starting from the simulated scanning beams we calculated their beam $a_{\ell m}$ using `beam2alm` with `beam_lmax` = 5400 and `beam_mmax` = 14. The sky $a_{\ell m}$ were convolved with the beam $a_{\ell m}$ using `conviqt_v3` with `conv_lmax` = 3000, `lmax_out` = 3000, `beammmax` = 14. The output is a "ringset" table for each realization, i.e., a grid of observed sky signal values for 6001 values of ϕ, 3002 values of θ and for 29 beam orientations (ψ). Note that the main beams do not collect the full power of the signal, since a small part of the signal spills outside the main beam to form sidelobes. In this MC just the main beam was simulated, not the sidelobes, so the calculated signal values were missing that part of the power that goes to the sidelobes. This was taken into account at the map-making stage.

The CMB timelines for each realization were produced with `multimod`. The detector pointing (ϕ, θ, ψ) for each radiometer was reconstructed internally using satellite pointing information and the focal plane geometry. The observed CMB signal for each sample was interpolated in θ and ϕ from the "ringset" table for its pointing using `interpol_order` = 9 (the effect of beam orientation ψ is solved exactly by `multimod` for the `beammmax` representation of the beam) and output to CMB timeline files. The detector pointing reconstructed by `multimod` was also output to disk for the use of the `Madam` map-maker. The reconstructed pointing was compared to the pointing used at the LFI DPC for the flight data maps to check that their agreement was satisfactory. There is an option in `multimod`, "sampler", to simulate the scanning motion of the radiometer during measurement of one observation sample. This, however, increases the computational cost so much that we turned this sampler off, and simulated this scanning motion by using the scanning beams (see above) instead of the optical beams.

Maps were made from these CMB timelines with `Madam` using the reconstructed pointing. The same `Madam` parameter settings were used as for the flight maps, see Zacchei et al. (2011) and Planck Collaboration II (2013). As already discussed in Sect. 4, the calibration step was not simulated.

References

Burigana, C., Natoli, P., Vittorio, N., Mandolesi, N., & Bersanelli, M. 2001, Experimental Astronomy, 12, 87
D'Arcangelo, O., Simonetto, A., Figini, L., et al. 2009, Journal of Instrumentation, 4, 2005
Górski, K. M., Hivon, E., Banday, A. J., et al. 2005, ApJ, 622, 759
Hill, R. S., Weiland, J. L., Odegard, N., et al. 2009, ApJS, 180, 246
Hivon, E., Górski, K. M., Netterfield, C. B., et al. 2002, ApJ, 567, 2
Huffenberger, K. M., Crill, B. P., Lange, A. E., Górski, K. M., & Lawrence, C. R. 2010, A&A, 510, A58+
Keihänen, E., Keskitalo, R., Kurki-Suonio, H., Poutanen, T., & Sirviö, A. 2010, A&A, 510, A57+
Keihanen, E. & Reinecke, M. 2012, Astronomy and Astrophysics, 548
Kurki-Suonio, H., Keihänen, E., Keskitalo, R., et al. 2009, A&A, 506, 1511
Mennella, A., Butler, R. C., Curto, A., et al. 2011, A&A, 536, A3
Mitra, S., Rocha, G., Górski, K. M., et al. 2011, ApJS, 193, 5
Nolta, M. R., Dunkley, J., Hill, R. S., et al. 2009, ApJS, 180, 296
Page, L., Barnes, C., Hinshaw, G., et al. 2003, ApJS, 148, 39
Planck Collaboration. 2011, The Explanatory Supplement to the Planck Early Release Compact Source Catalogue (ESA)
Planck Collaboration ES. 2013, The Explanatory Supplement to the Planck 2013 results (ESA)
Planck Collaboration I. 2011, A&A, 536, A1
Planck Collaboration I. 2013, In preparation
Planck Collaboration II. 2011, A&A, 536, A2
Planck Collaboration II. 2013, In preparation
Planck Collaboration III. 2013, In preparation
Planck Collaboration IX. 2011, A&A, 536, A9
Planck Collaboration V. 2013, In preparation
Planck Collaboration VI. 2013, In preparation
Planck Collaboration VII. 2011, A&A, 536, A7
Planck Collaboration VII. 2013, In preparation
Planck Collaboration VIII. 2011, A&A, 536, A8
Planck Collaboration X. 2011, A&A, 536, A10
Planck Collaboration XI. 2011, A&A, 536, A11
Planck Collaboration XII. 2011, A&A, 536, A12
Planck Collaboration XIII. 2011, A&A, 536, A13
Planck Collaboration XIV. 2011, A&A, 536, A14
Planck Collaboration XIX. 2011, A&A, 536, A19
Planck Collaboration XV. 2011, A&A, 536, A15
Planck Collaboration XV. 2013, In preparation
Planck Collaboration XVI. 2011, A&A, 536, A16
Planck Collaboration XVII. 2011, A&A, 536, A17
Planck Collaboration XVIII. 2011, A&A, 536, A18
Planck Collaboration XX. 2011, A&A, 536, A20
Planck Collaboration XXI. 2011, A&A, 536, A21
Planck Collaboration XXII. 2011, A&A, 536, A22
Planck Collaboration XXIII. 2011, A&A, 536, A23
Planck Collaboration XXIV. 2011, A&A, 536, A24
Planck Collaboration XXV. 2011, A&A, 536, A25
Planck Collaboration XXVIII. 2013, In preparation
Planck HFI Core Team. 2011a, A&A, 536, A4
Planck HFI Core Team. 2011b, A&A, 536, A6
Reinecke, M., Dolag, K., Hell, R., Bartelmann, M., & Enßlin, T. A. 2006, A&A, 445, 373
Rocha, G., Pagano, L., Górski, K. M., et al. 2010, A&A, 513, A23+
Sandri, M., Villa, F., Bersanelli, M., et al. 2010, A&A, 520, A7+
Tauber, J. A., Norgaard-Nielsen, H. U., Ade, P. A. R., et al. 2010, A&A, 520, A2+
Zacchei, A., Maino, D., Baccigalupi, C., et al. 2011, A&A, 536, A5

[1] APC, AstroParticule et Cosmologie, Université Paris Diderot, CNRS/IN2P3, CEA/lrfu, Observatoire de Paris, Sorbonne Paris Cité, 10, rue Alice Domon et Léonie Duquet, 75205 Paris Cedex 13, France
[2] Aalto University Metsähovi Radio Observatory, Metsähovintie 114, FIN-02540 Kylmälä, Finland
[3] African Institute for Mathematical Sciences, 6-8 Melrose Road, Muizenberg, Cape Town, South Africa
[4] Agenzia Spaziale Italiana Science Data Center, c/o ESRIN, via Galileo Galilei, Frascati, Italy
[5] Agenzia Spaziale Italiana, Viale Liegi 26, Roma, Italy
[6] Astrophysics Group, Cavendish Laboratory, University of Cambridge, J J Thomson Avenue, Cambridge CB3 0HE, U.K.

Table A.1. Selected LFI beams analysis notation.

Symbol	Description
M, S	Main and Side radiometer arm
LOS frame	telescope's Line of Sight reference frame
θ, ϕ	polar coordinates in the LOS frame
$\theta_{\rm MB}, \phi_{\rm MB}$	polar coordinates in the main beam frame
u, v	cartesian dimensionless coordinates in the LOS frame
e	beam ellipticity
FWHM	full width half maximum
ψ_{ell}	beam orientation defined with respect to the x-axis of the LOS frame
ψ	polarization angle (angle between the detector's polarization axis and the local meridian)
$\sigma^{\rm b}_{\rm max}, \sigma^{\rm b}_{\rm max}$	standard deviation of the elliptical Gaussian
η	Main beam efficiency
$\tau(\nu)$	bandpass
$T^{\rm M}_{\rm A}$ ($T^{\rm S}_{\rm A}$)	detector output in antenna temperature for the M (S) radiometer in the main beam frame
$E^{\rm M}_{\rm cp}$ ($E^{\rm S}_{\rm cp}$)	co-polar electric field component of the beam in the M (S) radiometer
$E^{\rm M}_{\rm xp}$ ($E^{\rm S}_{\rm xp}$)	cross-polar electric field component of the beam in the M (S) radiometer
$\chi^{\rm omt}$	cross-polarization of the orthomode transducer
$\hat{\boldsymbol{p}}_{\rm t}$	pointing direction for time sample t
$\hat{\boldsymbol{r}}_{\rm i}$	i-pixel center direction
$A_{\rm ti}$	Pointing matrix for pixel i and time sample t
$B_{ij} \equiv \boldsymbol{B}$	Effective beam for pointing pixel i and beam pixel j
$b(\hat{\boldsymbol{r}}, \hat{\boldsymbol{p}})$	Scanning beam at a direction $\hat{\mathbf{r}} \equiv [\theta, \phi]$ with the pointing angles $\hat{\mathbf{p}}$
$b_{\rm opt}(\theta)$	optical beam profile
γ	polarization efficiency $\gamma = (1 - \epsilon)/(1 + \epsilon)$, being ϵ the cross-polar leakage
$\boldsymbol{w}$	polarization weight factor
$\Omega_{\rm scn}$	solid angle of the scanning beam
$\Omega_{\rm opt}$	solid angle of the optical beam
$\Omega_{\rm sim}$	solid angle of the simulated beam
$\Omega_{\rm eff}$	solid angle of the effective beam
$\rm FWHM_{eff}$	effective beam full width half maximum
W_ℓ	beam window function
Λ_k	eigenvalues of the covariance matrix
$\boldsymbol{V}_k$	eigenvectors of the covariance matrix

[7] CITA, University of Toronto, 60 St. George St., Toronto, ON M5S 3H8, Canada
[8] CNRS, IRAP, 9 Av. colonel Roche, BP 44346, F-31028 Toulouse cedex 4, France
[9] California Institute of Technology, Pasadena, California, U.S.A.
[10] Centre for Theoretical Cosmology, DAMTP, University of Cambridge, Wilberforce Road, Cambridge CB3 0WA U.K.
[11] Centro de Estudios de Física del Cosmos de Aragón (CEFCA), Plaza San Juan, 1, planta 2, E-44001, Teruel, Spain
[12] Computational Cosmology Center, Lawrence Berkeley National Laboratory, Berkeley, California, U.S.A.
[13] Consejo Superior de Investigaciones Científicas (CSIC), Madrid, Spain
[14] DSM/Irfu/SPP, CEA-Saclay, F-91191 Gif-sur-Yvette Cedex, France
[15] DTU Space, National Space Institute, Technical University of Denmark, Elektrovej 327, DK-2800 Kgs. Lyngby, Denmark
[16] Département de Physique Théorique, Université de Genève, 24, Quai E. Ansermet,1211 Genève 4, Switzerland
[17] Departamento de Física Fundamental, Facultad de Ciencias, Universidad de Salamanca, 37008 Salamanca, Spain
[18] Departamento de Física, Universidad de Oviedo, Avda. Calvo Sotelo s/n, Oviedo, Spain
[19] Department of Astronomy and Astrophysics, University of Toronto, 50 Saint George Street, Toronto, Ontario, Canada
[20] Department of Astrophysics/IMAPP, Radboud University Nijmegen, P.O. Box 9010, 6500 GL Nijmegen, The Netherlands
[21] Department of Electrical Engineering and Computer Sciences, University of California, Berkeley, California, U.S.A.
[22] Department of Physics & Astronomy, University of British Columbia, 6224 Agricultural Road, Vancouver, British Columbia, Canada
[23] Department of Physics and Astronomy, Dana and David Dornsife College of Letter, Arts and Sciences, University of Southern California, Los Angeles, CA 90089, U.S.A.
[24] Department of Physics and Astronomy, University College London, London WC1E 6BT, U.K.
[25] Department of Physics, Gustaf Hällströmin katu 2a, University of Helsinki, Helsinki, Finland
[26] Department of Physics, Princeton University, Princeton, New Jersey, U.S.A.
[27] Department of Physics, University of California, One Shields Avenue, Davis, California, U.S.A.
[28] Department of Physics, University of California, Santa Barbara, California, U.S.A.
[29] Department of Physics, University of Illinois at Urbana-Champaign, 1110 West Green Street, Urbana, Illinois, U.S.A.
[30] Dipartimento di Fisica e Astronomia G. Galilei, Università degli Studi di Padova, via Marzolo 8, 35131 Padova, Italy
[31] Dipartimento di Fisica e Scienze della Terra, Università di Ferrara, Via Saragat 1, 44122 Ferrara, Italy
[32] Dipartimento di Fisica, Università La Sapienza, P. le A. Moro 2, Roma, Italy
[33] Dipartimento di Fisica, Università degli Studi di Milano, Via Celoria, 16, Milano, Italy
[34] Dipartimento di Fisica, Università degli Studi di Trieste, via A. Valerio 2, Trieste, Italy
[35] Dipartimento di Fisica, Università di Roma Tor Vergata, Via della Ricerca Scientifica, 1, Roma, Italy

[36] Discovery Center, Niels Bohr Institute, Blegdamsvej 17, Copenhagen, Denmark
[37] Dpto. Astrofísica, Universidad de La Laguna (ULL), E-38206 La Laguna, Tenerife, Spain
[38] European Space Agency, ESAC, Planck Science Office, Camino bajo del Castillo, s/n, Urbanización Villafranca del Castillo, Villanueva de la Cañada, Madrid, Spain
[39] European Space Agency, ESTEC, Keplerlaan 1, 2201 AZ Noordwijk, The Netherlands
[40] Haverford College Astronomy Department, 370 Lancaster Avenue, Haverford, Pennsylvania, U.S.A.
[41] Helsinki Institute of Physics, Gustaf Hällströmin katu 2, University of Helsinki, Helsinki, Finland
[42] INAF - Osservatorio Astrofisico di Catania, Via S. Sofia 78, Catania, Italy
[43] INAF - Osservatorio Astronomico di Padova, Vicolo dell'Osservatorio 5, Padova, Italy
[44] INAF - Osservatorio Astronomico di Roma, via di Frascati 33, Monte Porzio Catone, Italy
[45] INAF - Osservatorio Astronomico di Trieste, Via G.B. Tiepolo 11, Trieste, Italy
[46] INAF/IASF Bologna, Via Gobetti 101, Bologna, Italy
[47] INAF/IASF Milano, Via E. Bassini 15, Milano, Italy
[48] INFN, Sezione di Bologna, Via Irnerio 46, I-40126, Bologna, Italy
[49] INFN, Sezione di Roma 1, Università di Roma Sapienza, Piazzale Aldo Moro 2, 00185, Roma, Italy
[50] IPAG: Institut de Planétologie et d'Astrophysique de Grenoble, Université Joseph Fourier, Grenoble 1 / CNRS-INSU, UMR 5274, Grenoble, F-38041, France
[51] ISDC Data Centre for Astrophysics, University of Geneva, ch. d'Ecogia 16, Versoix, Switzerland
[52] IUCAA, Post Bag 4, Ganeshkhind, Pune University Campus, Pune 411 007, India
[53] Imperial College London, Astrophysics group, Blackett Laboratory, Prince Consort Road, London, SW7 2AZ, U.K.
[54] Infrared Processing and Analysis Center, California Institute of Technology, Pasadena, CA 91125, U.S.A.
[55] Institut Néel, CNRS, Université Joseph Fourier Grenoble I, 25 rue des Martyrs, Grenoble, France
[56] Institut Universitaire de France, 103, bd Saint-Michel, 75005, Paris, France
[57] Institut d'Astrophysique Spatiale, CNRS (UMR8617) Université Paris-Sud 11, Bâtiment 121, Orsay, France
[58] Institut d'Astrophysique de Paris, CNRS (UMR7095), 98 bis Boulevard Arago, F-75014, Paris, France
[59] Institute for Space Sciences, Bucharest-Magurale, Romania
[60] Institute of Astronomy and Astrophysics, Academia Sinica, Taipei, Taiwan
[61] Institute of Astronomy, University of Cambridge, Madingley Road, Cambridge CB3 0HA, U.K.
[62] Institute of Theoretical Astrophysics, University of Oslo, Blindern, Oslo, Norway
[63] Instituto de Astrofísica de Canarias, C/Vía Láctea s/n, La Laguna, Tenerife, Spain
[64] Instituto de Física de Cantabria (CSIC-Universidad de Cantabria), Avda. de los Castros s/n, Santander, Spain
[65] Istituto di Fisica del Plasma, CNR-ENEA-EURATOM Association, Via R. Cozzi 53, Milano, Italy
[66] Jet Propulsion Laboratory, California Institute of Technology, 4800 Oak Grove Drive, Pasadena, California, U.S.A.
[67] Jodrell Bank Centre for Astrophysics, Alan Turing Building, School of Physics and Astronomy, The University of Manchester, Oxford Road, Manchester, M13 9PL, U.K.
[68] Kavli Institute for Cosmology Cambridge, Madingley Road, Cambridge, CB3 0HA, U.K.
[69] LAL, Université Paris-Sud, CNRS/IN2P3, Orsay, France
[70] LERMA, CNRS, Observatoire de Paris, 61 Avenue de l'Observatoire, Paris, France
[71] Laboratoire AIM, IRFU/Service d'Astrophysique - CEA/DSM - CNRS - Université Paris Diderot, Bât. 709, CEA-Saclay, F-91191 Gif-sur-Yvette Cedex, France
[72] Laboratoire Traitement et Communication de l'Information, CNRS (UMR 5141) and Télécom ParisTech, 46 rue Barrault F-75634 Paris Cedex 13, France
[73] Laboratoire de Physique Subatomique et de Cosmologie, Université Joseph Fourier Grenoble I, CNRS/IN2P3, Institut National Polytechnique de Grenoble, 53 rue des Martyrs, 38026 Grenoble cedex, France
[74] Laboratoire de Physique Théorique, Université Paris-Sud 11 & CNRS, Bâtiment 210, 91405 Orsay, France
[75] Lawrence Berkeley National Laboratory, Berkeley, California, U.S.A.
[76] Max-Planck-Institut für Astrophysik, Karl-Schwarzschild-Str. 1, 85741 Garching, Germany
[77] McGill Physics, Ernest Rutherford Physics Building, McGill University, 3600 rue University, Montréal, QC, H3A 2T8, Canada
[78] MilliLab, VTT Technical Research Centre of Finland, Tietotie 3, Espoo, Finland
[79] Niels Bohr Institute, Blegdamsvej 17, Copenhagen, Denmark
[80] Observational Cosmology, Mail Stop 367-17, California Institute of Technology, Pasadena, CA, 91125, U.S.A.
[81] SB-ITP-LPPC, EPFL, CH-1015, Lausanne, Switzerland
[82] SISSA, Astrophysics Sector, via Bonomea 265, 34136, Trieste, Italy
[83] School of Physics and Astronomy, Cardiff University, Queens Buildings, The Parade, Cardiff, CF24 3AA, U.K.
[84] School of Physics and Astronomy, University of Nottingham, Nottingham NG7 2RD, U.K.
[85] Space Sciences Laboratory, University of California, Berkeley, California, U.S.A.
[86] Special Astrophysical Observatory, Russian Academy of Sciences, Nizhnij Arkhyz, Zelenchukskiy region, Karachai-Cherkessian Republic, 369167, Russia
[87] Stanford University, Dept of Physics, Varian Physics Bldg, 382 Via Pueblo Mall, Stanford, California, U.S.A.
[88] Sub-Department of Astrophysics, University of Oxford, Keble Road, Oxford OX1 3RH, U.K.
[89] Theory Division, PH-TH, CERN, CH-1211, Geneva 23, Switzerland
[90] UPMC Univ Paris 06, UMR7095, 98 bis Boulevard Arago, F-75014, Paris, France
[91] Université de Toulouse, UPS-OMP, IRAP, F-31028 Toulouse cedex 4, France
[92] University of Granada, Departamento de Física Teórica y del Cosmos, Facultad de Ciencias, Granada, Spain
[93] University of Miami, Knight Physics Building, 1320 Campo Sano Dr., Coral Gables, Florida, U.S.A.
[94] Warsaw University Observatory, Aleje Ujazdowskie 4, 00-478 Warszawa, Poland

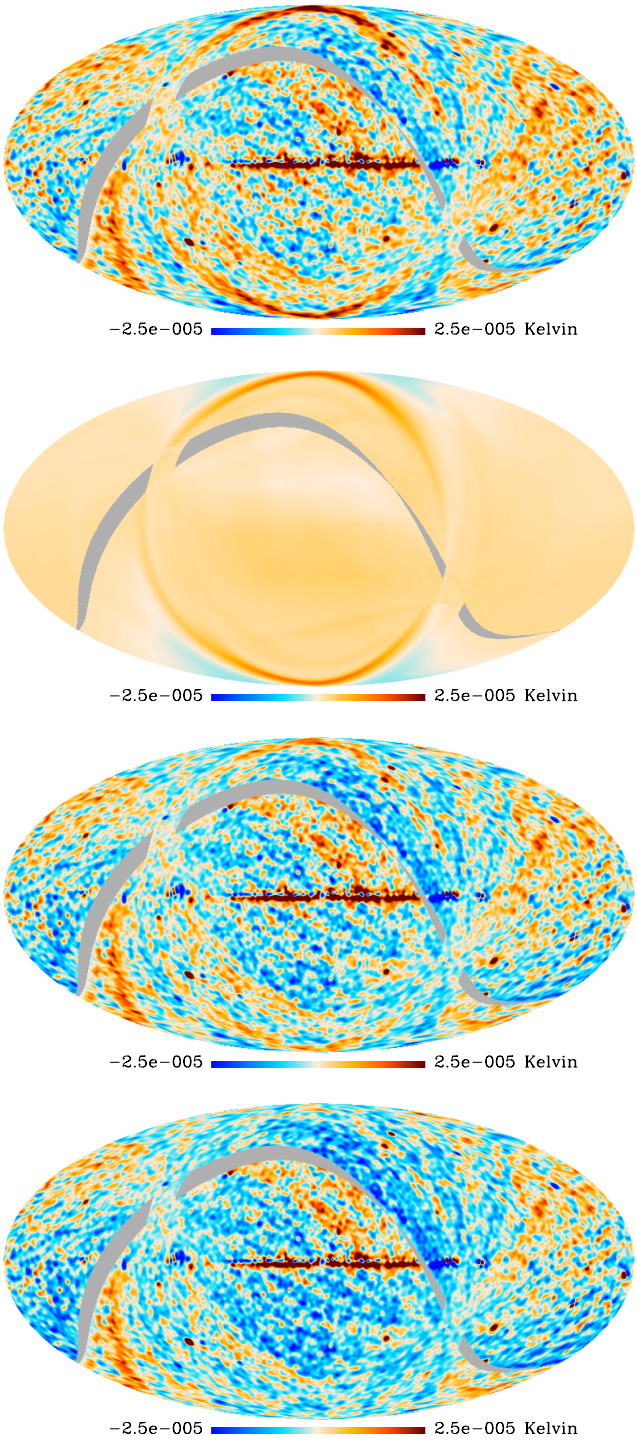

Fig. 9. Survey 1 – Survey 2 difference maps. *Top*: 30 GHz map, in μK. *Second*: simulated Galactic straylight. *Third*: data minus simulations. The ring still visible in the third panel suggests that the model should be improved by adding higher order contributions, possibly combined with physical optics analyses. *Bottom*: difference between data and simulations, amplified by a factor equal to the ratio of the power missing the main beam ($f_{\rm sl}$) and the power entering the simulated sidelobes using the first order approximation (in this case, about 1.93). The grey-band is a lack of data.

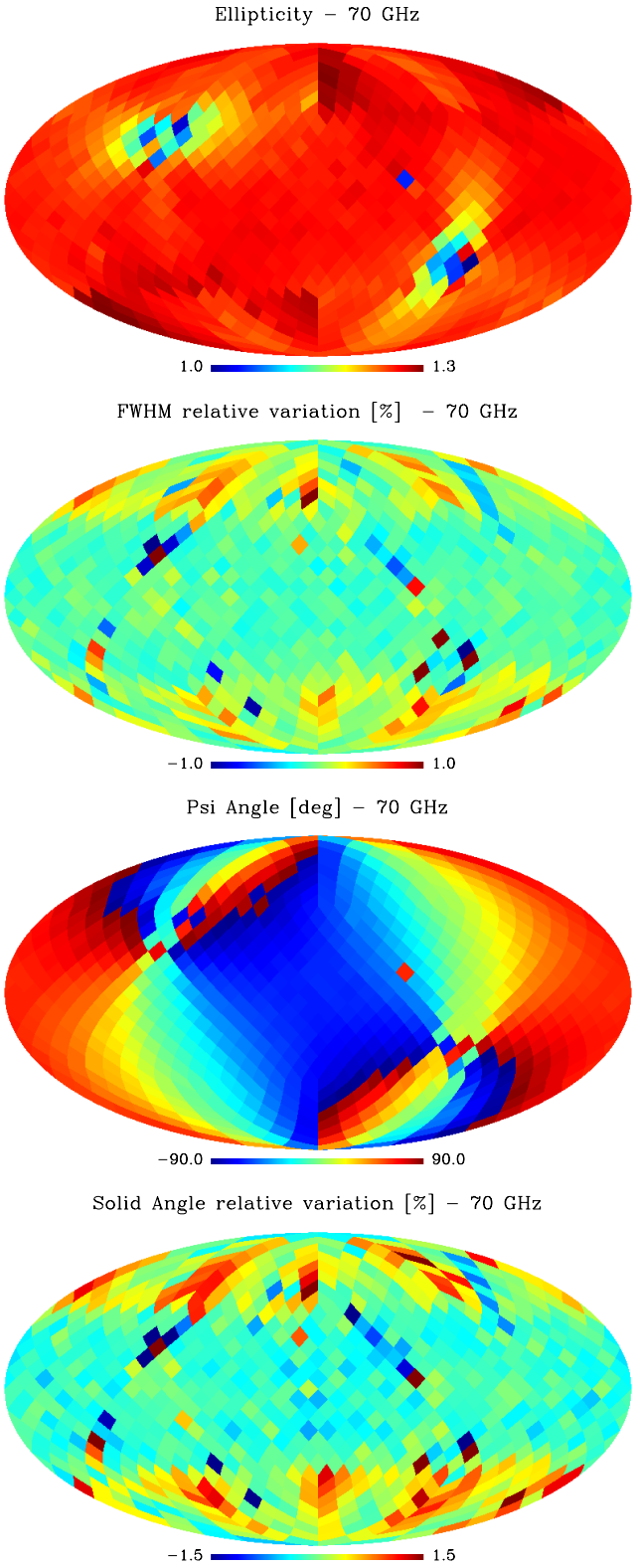

Fig. 10. Main parameters of the LFI effective beams: ellipticity (first row); FWHM (relative variation with respect to the FWHM of the scanning main beam, second row); ψ (third row); and beam solid angle (relative variation with respect to the scanning main beam solid angle reported in Table 2, fourth row), for the 70 GHz channel.

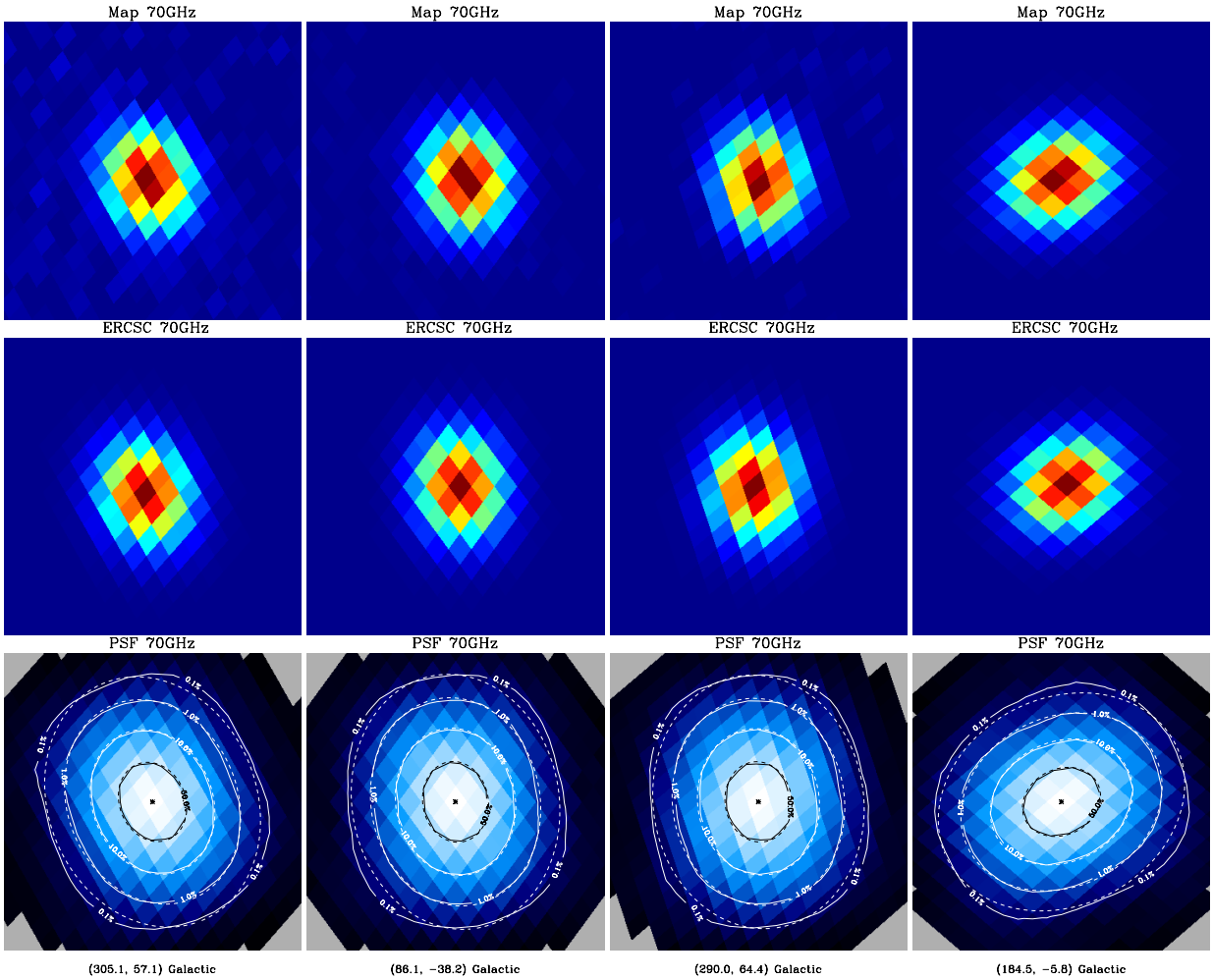

Fig. 11. Four ERCSC sources as seen by LFI 70 GHz channel (upper panel); linear scale FEBeCoP PSFs computed using input simulated beams (central panel); both in arbitrary units. Bottom panel: PSF iso-contours shown in solid line, elliptical Gaussian fit iso-contours shown in broken line. PSFs are shown in log scale.

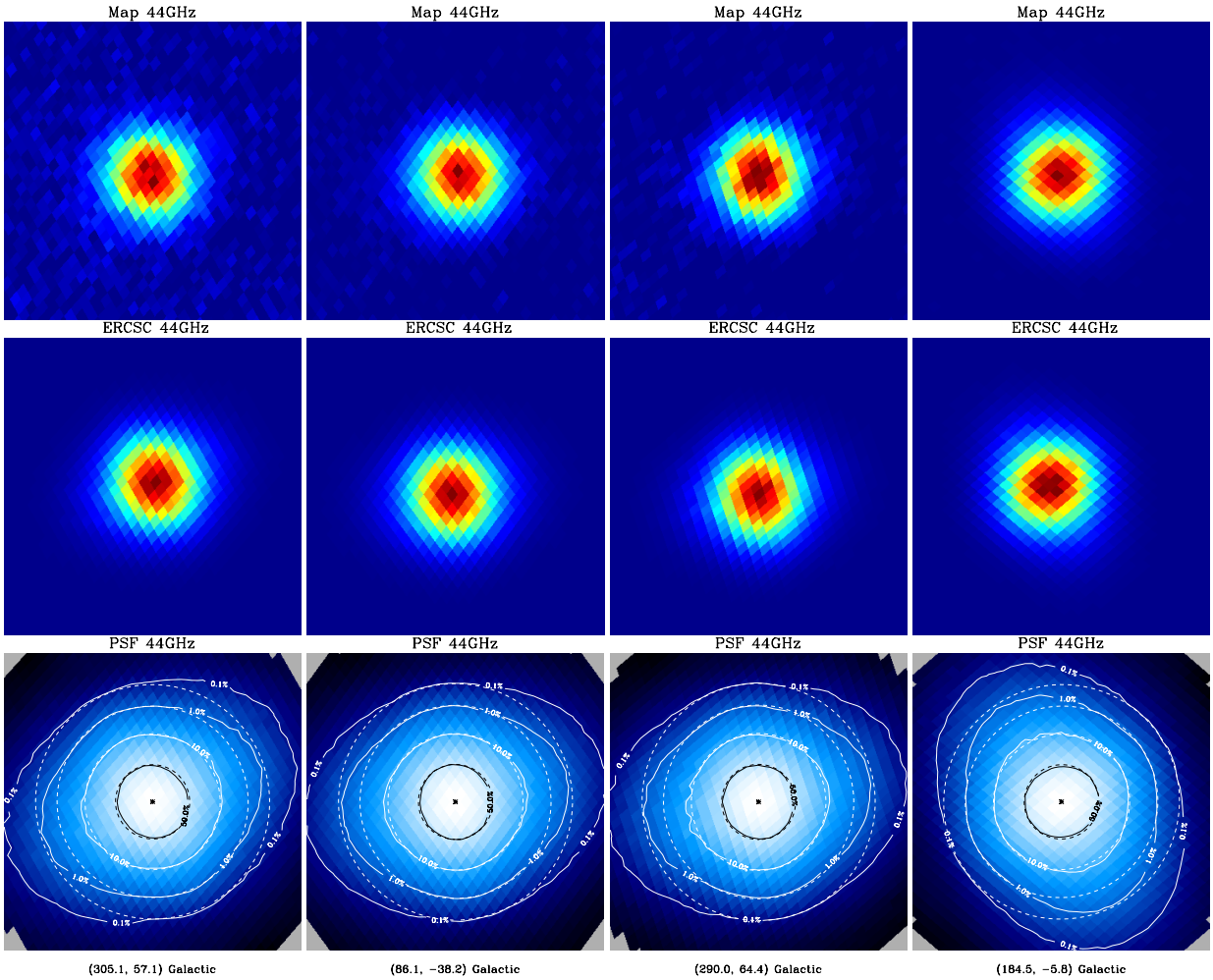

Fig. 12. Four ERCSC sources as seen by LFI 44 GHz channel (upper panel); linear scale FEBeCoP PSFs computed using input simulated beams (central panel); both in arbitrary units. Bottom panel: PSF iso-contours shown in solid line, elliptical Gaussian fit iso-contours shown in broken line. PSFs are shown in log scale.

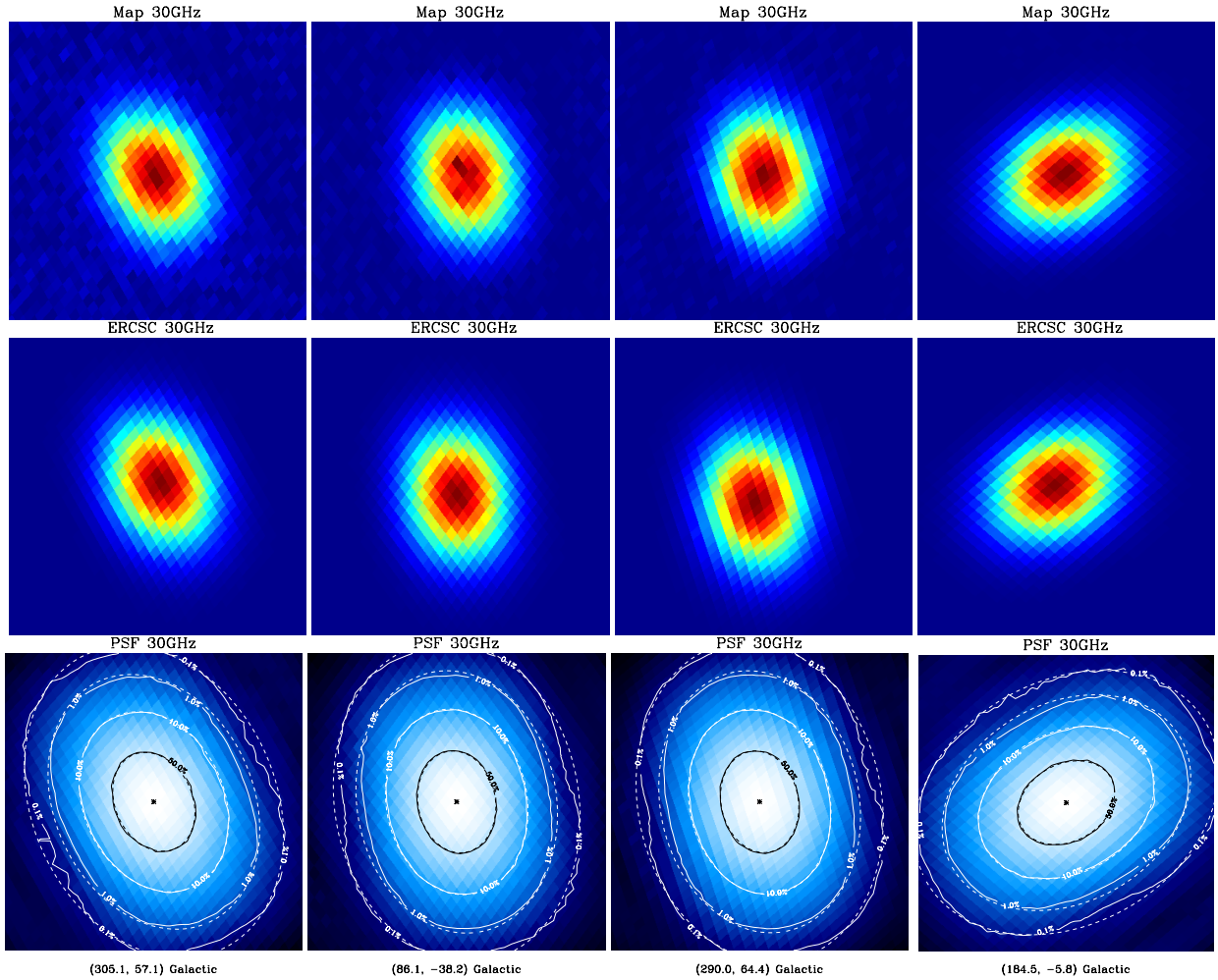

Fig. 13. Four ERCSC sources as seen by LFI 30 GHz channel (upper panel); linear scale FEBeCoP PSFs computed using input simulated beams (central panel); both in arbitrary units. Bottom panel: PSF iso-contours shown in solid line, elliptical Gaussian fit iso-contours shown in broken line. PSFs are shown in log scale.

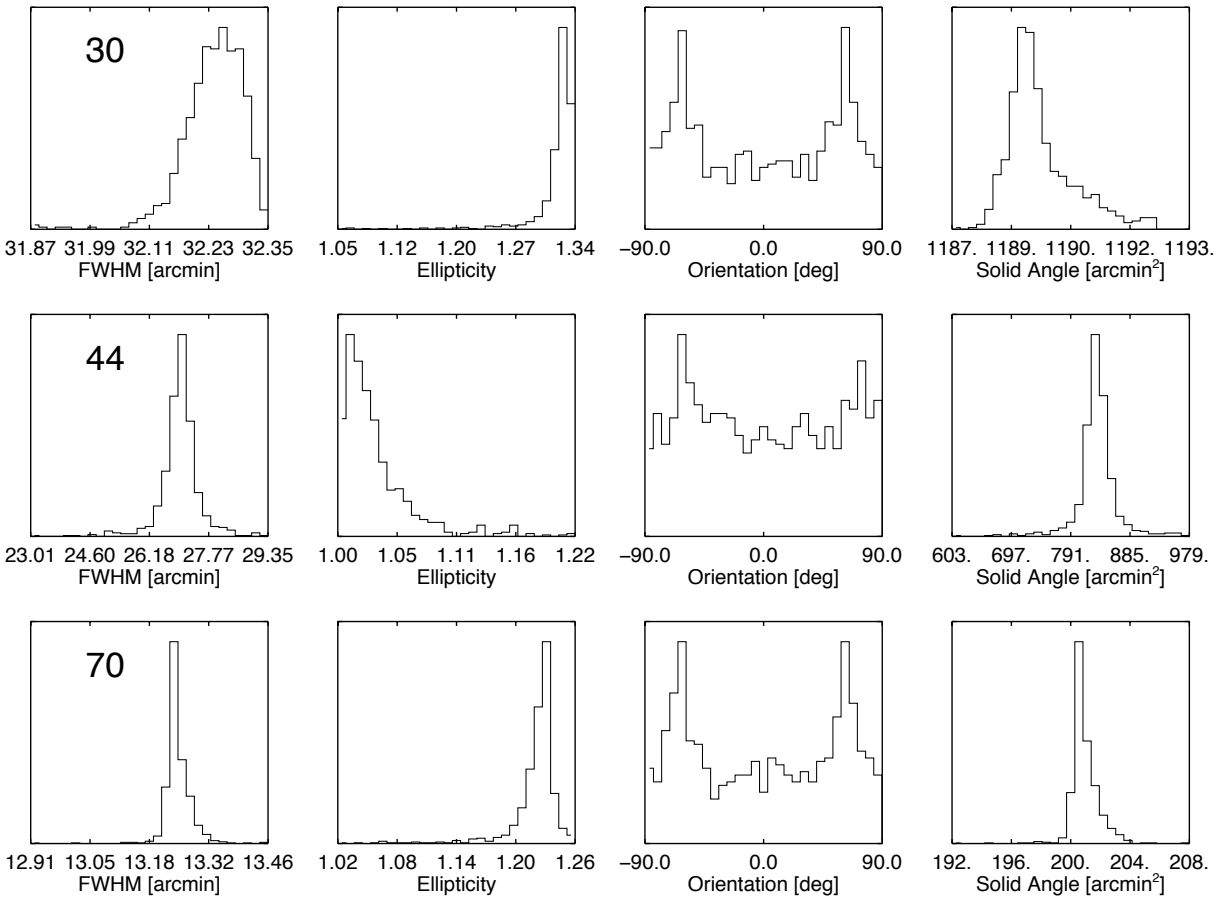

Fig. 14. Histograms of the three fit parameters (beam FWHM, ellipticity, and orientation with respect to the local meridian) for the effective beams computed using `FEBeCoP` with the simulated beams. We sampled the sky (fairly sparsely) at 768 directions, chosen as `HEALpix` N_{side}=8 pixel centres to uniformly sample the sky.

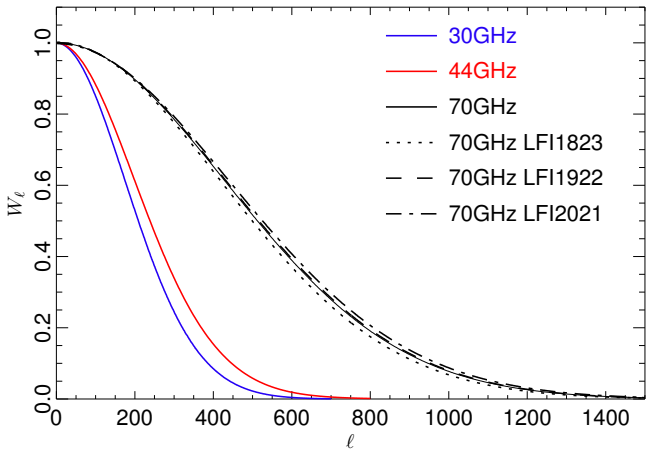

Fig. 15. Timeline-to-map, Monte Carlo-based beam window functions for *Planck* 30, 44, and 70 GHz frequency maps. For 70 GHz, we also show the beam window functions for a subset of paired horns, namely `LFI18-23`, `LFI19-22`, and `LFI20-21`.

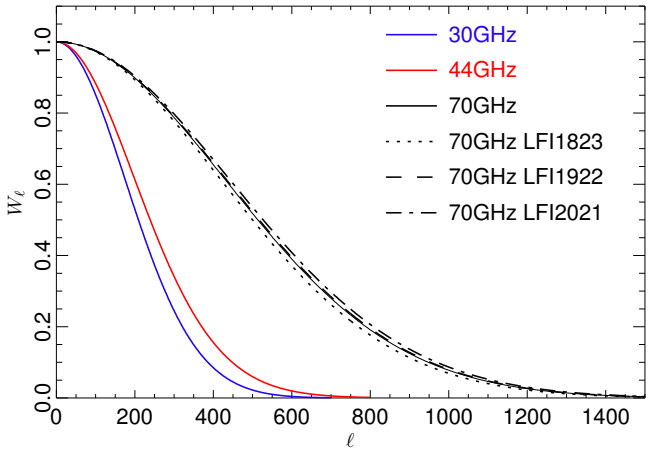

Fig. 16. `FEBeCoP` beam window functions for *Planck* 30, 44, and 70 GHz frequency maps. For 70 GHz, we also show the beam window functions for a subset of detectors, namely `LFI18-23`, `LFI19-22`, and `LFI20-21`.

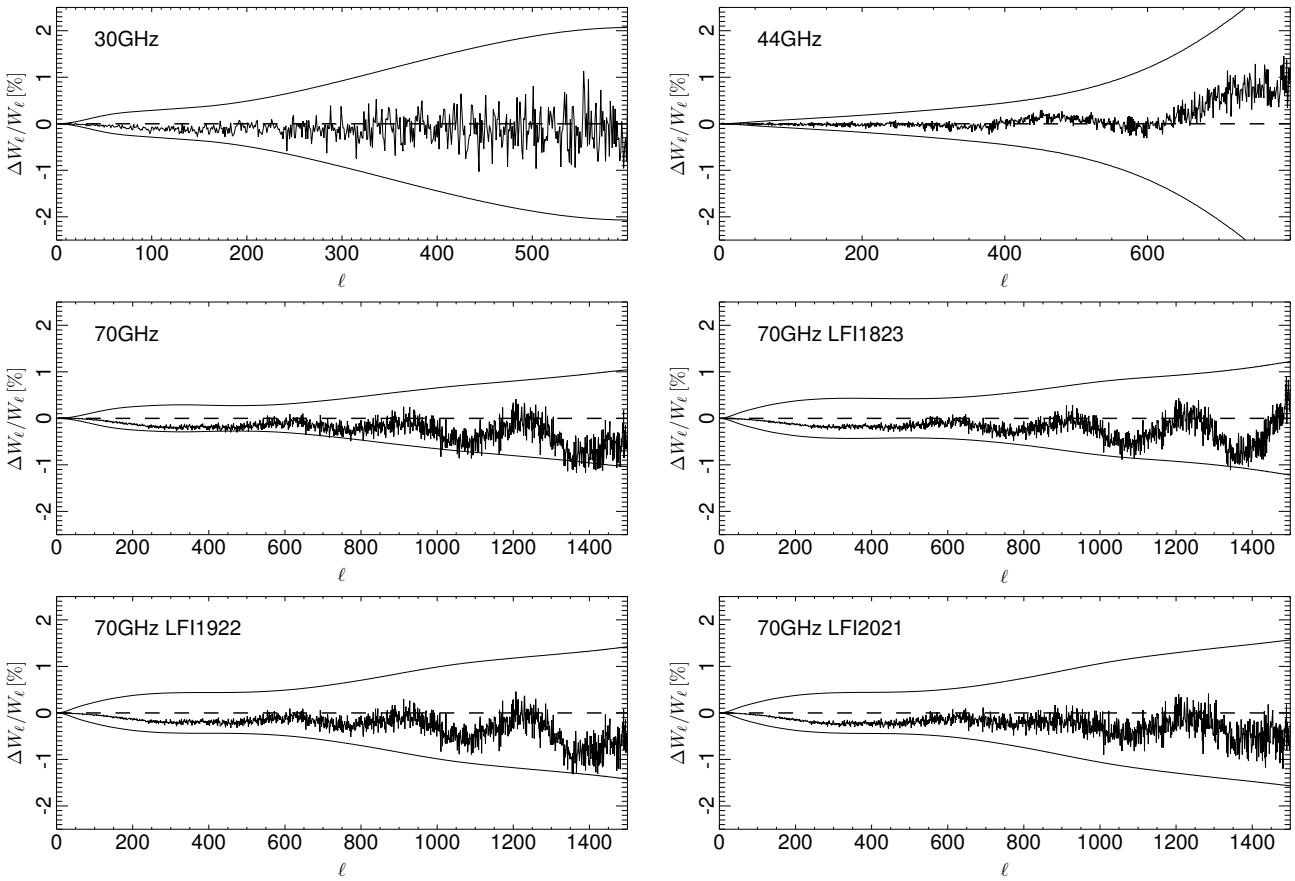

Fig. 17. Comparison between timeline-to-map MC-based and FEBeCoP beam window functions. We also show the $\pm 1\sigma$ error envelopes obtained in Sec. 5.

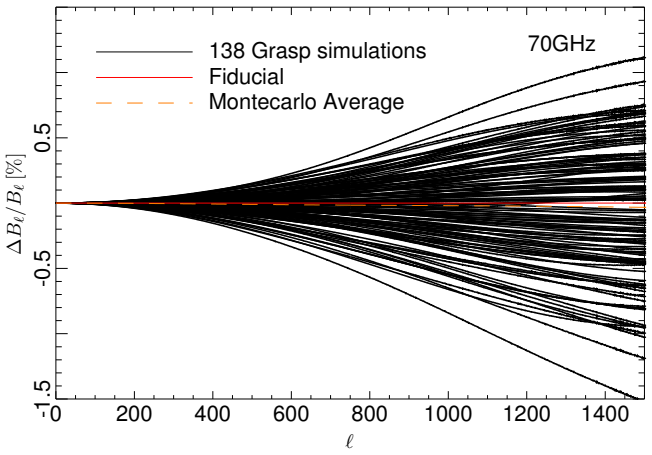

Fig. 18. Beam window functions generated and normalized to the fiducial.

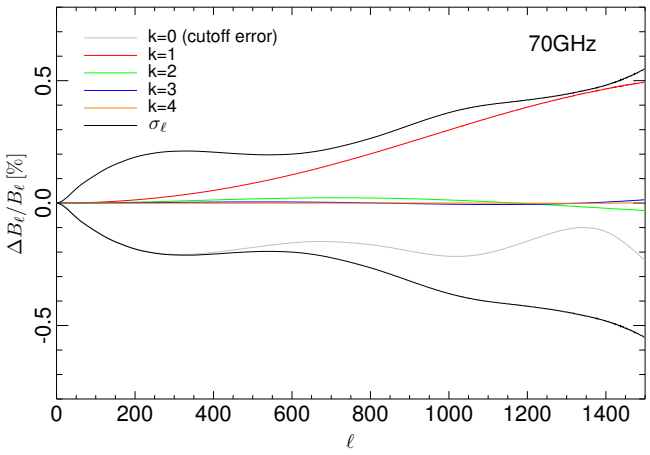

Fig. 21. First four eigenmodes of the covariance matrix of the 70 GHz channel.

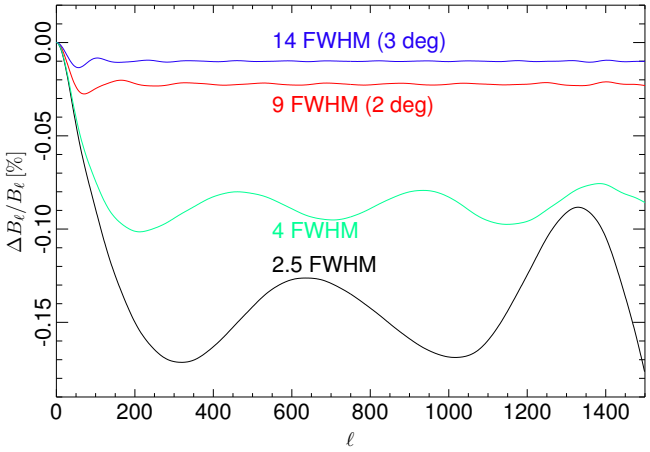

Fig. 19. Relative difference between B_ℓs computed for various cutoff values and the one with full integration. All the functions have been computed using eq. 14 for a symmetrized version of the `LFI18M` beam profile.

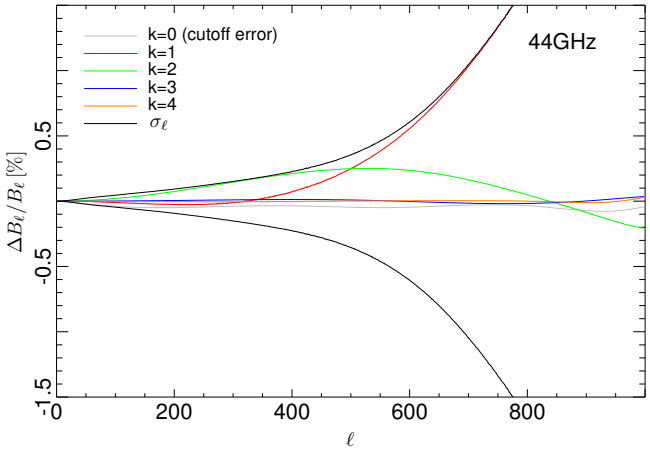

Fig. 22. First four eigenmodes of the covariance matrix of the 44 GHz channel.

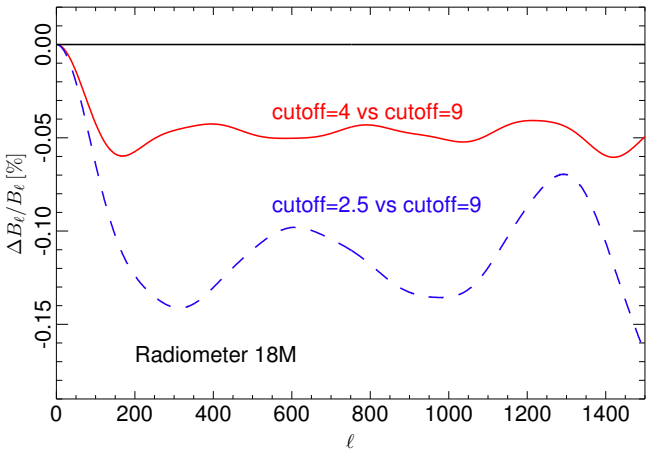

Fig. 20. Same as Fig. 19, but the window functions have been computed with `FEBeCoP`.

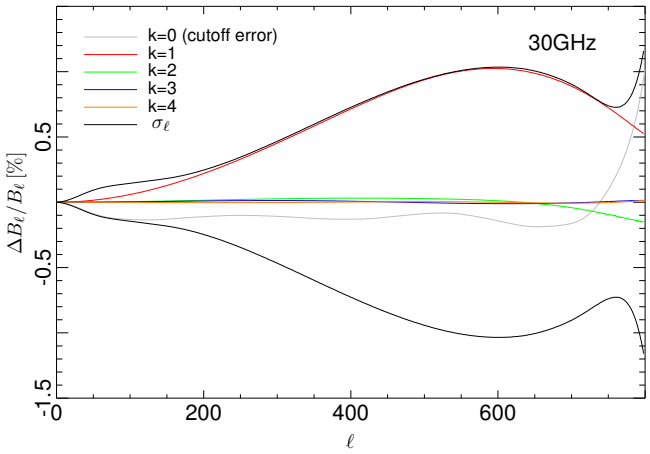

Fig. 23. First four eigenmodes of the covariance matrix of the 30 GHz channel.